LOW-TEMPERATURE GROWN III-V MATERIALS

M. R. Melloch, J. M. Woodall, and E. S. Harmon

School of Electrical Engineering and the MRSEC for Technology-Enabling Heterostructure Materials, Purdue University, West Lafayette, Indiana 47907–1285

N. Otsuka

School of Materials Science, Japan Advanced Institute of Science and Technology, Hokuriku, Nomigun, Ishikawa 923–12, Japan

Fred H. Pollak

Department of Physics, Brooklyn College of the City of New York, Brooklyn, New York 11210

D. D. Nolte

Department of Physics and the MRSEC for Technology-Enabling Heterostructure Materials, Purdue University, West Lafayette, Indiana 47907–1285

R. M. Feenstra and M. A. Lutz

IBM Research Division, T. J. Watson Research Center, Yorktown Heights, New York 10598

ABSTRACT

A new kind of semiconductor composite material is demonstrated with a dispersion of semimetallic particles with properties common to high-

quality single crystals. These materials are arsenides such as GaAs, AlGaAs, and InGaAs containing arsenic clusters. The composites are formed by incorporating excess arsenic in the semiconductor, which percipitates in the anneal. The incorporation of the excess arsenic is accomplished by molecular beam epitaxy at low substrate temperatures. The cluster density can be controlled with the coarsening annealing. The positioning of the clusters can be controlled with heterojunctions and doping. These composites exhibit several interesting properties, including high-resistivity, appreciable optical absorption below the band gap of the semiconductor matrix material, a large electro-optic effect, and very short carrier lifetimes.

INTRODUCTION

Molecular beam epitaxy (MBE) is a film growth technique where atomic or molecular beams are thermally evaporated onto a heated substrate in an ultra-high vacuum (1). The ultra-high vacuum allows monitoring of the growth with techniques such as reflection high-energy electron diffraction (RHEED) (2) and desorption mass spectroscopy (3). By far the largest application of MBE has been for the growth of III-V materials, especially the arsenides. Typical MBE systems have eight ports for effusion furnaces for evaporation of source material. Typical group III sources are gallium, aluminum, and indium. The dominant group V source is arsenic, although antimony and phosphorous sources are not atypical. Arsenic sublimes as a tetramer molecule As_4. Often the arsenic effusion furnace is equipped with a cracking zone that results in dimer molecules of As_2. Silicon is used for the n-type dopant and beryllium for the p-type dopant almost exclusively for III-V MBE. The typical conditions for MBE of high-quality GaAs are a substrate temperature of 600°C, an As_4-to-Ga beam equivalent pressure (bep) ratio of 15–20, and a growth rate of 1 μm/h. (The bep is measured with an ion gauge in the growth position.) With the Ga effusion furnace at a temperature near 900°C to obtain a 1 μm/h growth rate, every Ga atom that impinges on the substrate at a temperature of 600°C will remain and have enough thermal energy to find a lattice site. The arsenic molecules, originating from an effusion furnace at a temperature of about 250°C, will only result in the incorporation of an arsenic atom if there is a Ga atom to bond to. Therefore, the MBE of arsenides readily lends itself to the growth of highly stoichiometric material. During the last six years there has been considerable interest in the MBE of arsenides at lower substrate temperatures—as low as 200°C. As described below, this has made possible the growth of nonstoichiometric material of high crystal quality, which has many interesting and useful properties.

One of the first applications of a GaAs epilayer grown at low substrate temperatures by MBE was by Murotani et al (4). They were investigating the MBE of GaAs on substrates with a temperature range of 400 to 600°C and found that the material became semi-insulating below a critical substrate temperature—which had obvious applications for buffer layers for MESFETs—so they placed such a buffer layer under a GaAs power metal-semiconductor field-effect transistor (MESFET) (4). This application received little notice until 1988 when Smith et al (5) investigated the use of GaAs grown in the neighborhood of 200°C as a buffer layer under a MESFET and found that it completely eliminated the problem of sidegating. Melloch et al (6) then showed that state-of-the-art high electron mobility transistor (HEMT) material could be grown on top of GaAs buffer layers grown at extremely low substrate temperatures (250°C) and that such buffer layers might have the beneficial effect of slowing diffusion of impurities from the substrate toward the active layers.

There has been an enormous amount of research since 1988 on the MBE of arsenides grown at low substrate temperatures. These materials are usually referred to in the literature as (low-temperature) LT-GaAs. The adoption of the term LT-GaAs is unfortunate because those not familiar with the field obviously assume one is referring to properties of GaAs at low temperatures, not to new materials that exhibit new physics with exciting electronic and optoelectronic device possibilities. The term LT-GaAs also has been used to refer to a broad range of materials whose only thread of commonality is the initial processing step of MBE at low substrate temperatures. As-grown materials are highly nonstoichiometric with the excess arsenic in the form of point defects (7). With sufficient anneal, the nature of the material changes completely, with the excess arsenic precipitating to form semi-metallic arsenic clusters in a GaAs semiconductor matrix (8). Therefore, better terminology would be low-temperature grown (LTG) GaAs to refer only to the as-grown material, and GaAs:As or metal/semiconductor composite to refer to the annealed material.

There have been a number of controversies surrounding LTG-GaAs. The initial controversy was concerned with what happened to the excess arsenic after anneal. First reports of transmission electron microscopy (TEM) of these materials indicated that after anneal the LTG-GaAs epilayers were devoid of any obvious defects (9). However, it is now known that the excess arsenic precipitates during annealing (8, 10–19). Another controversy surrounding LTG-GaAs was a report that the material was superconducting (20). However, it is believed this report was related to the indium used for mounting the substrate during MBE.

Some controversy still remains about the role of residual defects vs

arsenic clusters in controlling the material properties (21–26). Part of the debate is whether the arsenic clusters act as embedded Schottky contacts. There is considerable supporting evidence from measurement techniques such as transmission electron microscopy (TEM), scanning tunneling microscopy (STM), and others that the arsenic clusters are indeed embedded Schottky contacts. Transmission electron diffraction clearly indicates the crystal structure of the arsenic clusters as hexagonal (8), the semi-metallic form for arsenic. STM current-voltage spectroscopy reveals a depletion region around the arsenic precipitates in annealed LTG-n-GaAs, indicating that the arsenic clusters are acting as buried Schottky barriers (27). Obviously, the properties of as-grown material are dominated by point defects, but as one anneals, the role of defects (which are disappearing) will decrease, whereas the role of the arsenic clusters (which are precipitating) will increase. Another part of the controversy of the role of point defects vs arsenic clusters arises because of this gradual transition and from drawing global conclusions without investigating a spectrum of anneals that take the material from the point-defect-dominated form to the two-phase composite form.

In this article, we describe the fabrication of these materials, review the material properties as one transitions from the as-grown point-defect-dominated material to the annealed composite form, and look at many of the device applications that these new materials have already enabled.

ARSENIC CLUSTER ENGINEERING

Low-Substrate-Temperature Molecular Beam Epitaxy

In 1969, Cho (28) investigated MBE of GaAs at room temperature and found that the deposited material was amorphous, but that if the layer was thin enough, it would turn crystalline with annealing. Murotani et al (4) investigated the MBE of GaAs down to a substrate temperature of 400°C and found that the material remained crystalline and became semi-insulating below a critical temperature. Smith et al (5) investigated the MBE of GaAs in the neighborhood of 200°C, finding that it remained crystalline and that epilayers suitable for MESFETs could be grown on top of these LTG-GaAs epilayers. Eaglesham et al (29) have demonstrated epitaxy of GaAs down to substrate temperatures around 140°C. However, they found there is a critical thickness beyond which the film turns amorphous. This critical thickness is a function of the amount of excess arsenic incorporated into the epilayer, which is a function of the substrate temperature (12, 30); the arsenic species-to-Ga flux ratio (29); and the arsenic species (the dimer As_2 or the tetramer As_4) used (10). GaAs epilayers as thick as 1 μm with 1.5% excess arsenic have been demonstrated (7, 8). Ibbetson et

al (31) have determined through their observation of RHEED oscillations that even at these low temperatures, MBE of GaAs is a layer-by-layer process. To observe the RHEED oscillations at these low substrate temperatures requires a smooth surface free of excess arsenic. Below 200°C the RHEED oscillations are very sensitive to the arsenic-to-Ga-flux ratio, the strongest oscillations being obtained under stoichiometric conditions.

The excess arsenic incorporated into GaAs during low-substrate-temperature MBE is in the form of point defects, such as arsenic antisites and possibly arsenic interstitials (7), and the epilayer is strained (7, 32, 33). The amount of excess arsenic can be controlled with the substrate temperature during MBE. The lower the substrate temperature, the greater is the amount of excess arsenic that is incorporated (12, 34). The double crystal rocking curve for a LTG-GaAs epilayer containing 1.5% excess arsenic is shown in Figure 1—a perpendicular mismatch of 0.133% is observed. What is remarkable about the rocking curve in Figure 1 is that although the epilayer was grown at a substrate temperature of 225°C and contains 1.5% excess arsenic, there is a clear presence of Pendellösung fringes. The Pendellösung fringes are caused by interference between the X-ray fields from the epilayer and the substrate. To observe these fringes, there must be a high degree of coherence between the two X-ray fields, indicating a high degree of structural quality for the epilayer (35). Most of the strain in LTG-GaAs is relaxed with modest anneals, e.g. 600°C for 10 to 30 min or 700°C or higher for 30 s or less (7, 32, 33). This strain relaxation is accompanied by precipitation of the excess arsenic (8). Figure 2 shows TEM images of two samples from a LTG-GaAs epilayer, one that was annealed for 30 s at 550°C and one that was annealed for 30 s at 900°C. Clearly seen in Figure 2 is a coarsening of the clusters with annealing; the sample that was annealed at 550°C for 30 s has a much higher density of smaller arsenic clusters than the sample annealed at 900°C for 30 s. This coarsening occurs because the two-phase system of the arsenic clusters in the GaAs matrix is minimizing its free energy with annealing by reducing the interfacial area between the arsenic precipitates and the GaAs matrix— an Ostwald ripening process (36). This process of incorporating excess arsenic followed by an anneal also has been used to obtain arsenic precipitates in AlGaAs (12) and InGaAs (17–19) semiconductor matrices. The wide range of control that one has over the structure of these composites is illustrated in Figure 3, where the average density and diameter of the arsenic clusters is shown as a function of temperature for a 30 s anneal for four different epilayers. Three of these epilayers are GaAs, one with 0.9% excess arsenic, one with 0.7% excess arsenic, and one with 0.3% excess arsenic. The fourth epilayer is $Al_{0.25}Ga_{0.75}As$ containing 0.3% excess
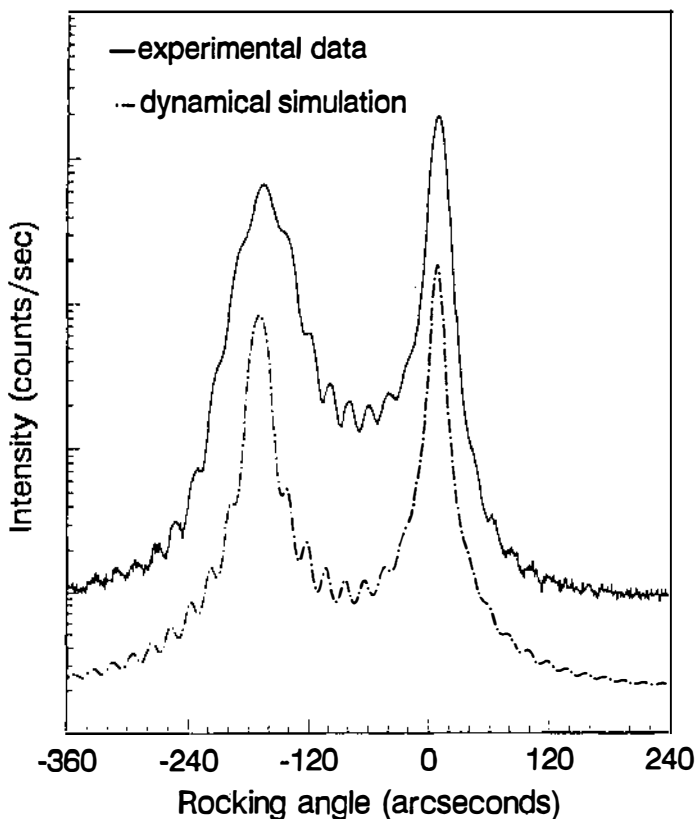
Figure 1 Experimental and calculated (004) double-crystal rocking curves for LTG-GaAs sample containing 1.5% excess arsenic.

arsenic. The amount of the excess arsenic in these epilayers was fixed by the substrate temperature during MBE.

Taking advantage of the strain relaxation that occurs with anneal, Melloch et al (15) have demonstrated a technique to grow arbitrarily thick LTG-GaAs layers. After growth of 2 μm of material, the substrate temperature was cycled to 600°C and then back to the growth temperature of 250°C. With this approach the strain is relaxed before the critical thickness is reached and LTG-GaAs with arbitrary thickness can be grown.

Extrinsic Control of Arsenic Clusters with Doping

When dopants are incorporated into LTG-GaAs, the arsenic cluster coarsening processes can be significantly affected. In MBE, the typical *n*-type dopant is Si and the typical *p*-type dopant is Be. For normal substrate
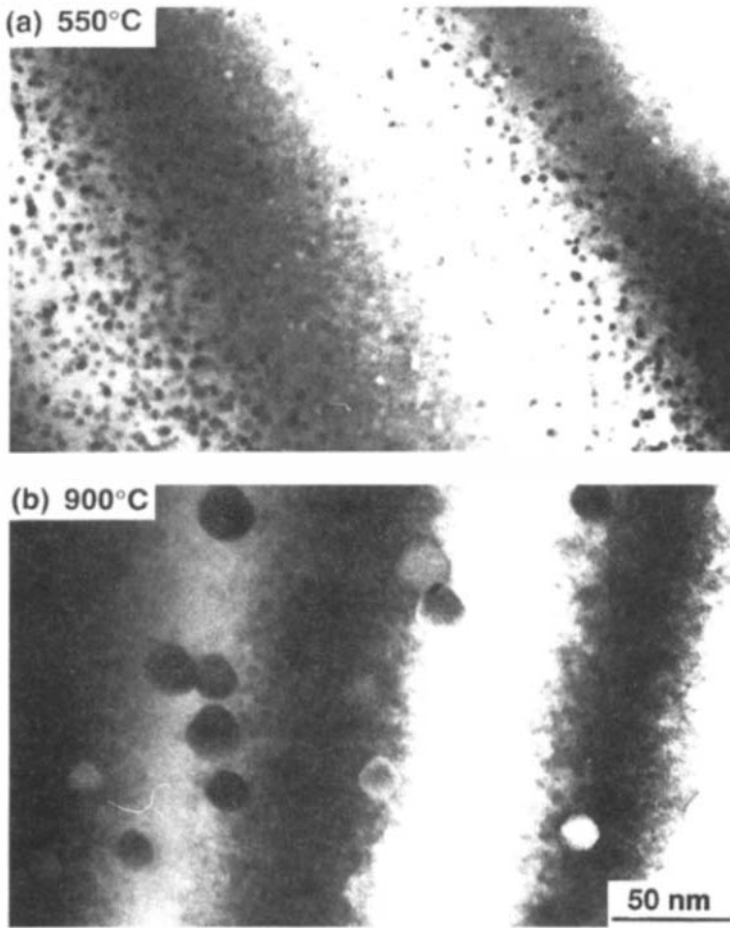
Figure 2 TEM images of two samples from the same LTG-GaAs epilayer that were annealed at (*a*) 550°C for 30 s and (*b*) 900°C for 30 s.

temperature (600°C) MBE, Si is incorporated as a donor for con-centrations up to low 10^{18} cm^{-3}. At higher concentrations, a significant amount of the Si is incorporated on the arsenic site and the material becomes compensated. As the substrate temperature is lowered from 600°C, the concentration of Si on donor sites (before compensation occurs) increases (37). When very low substrate temperatures are reached during MBE, there is uncertainty concerning the site for the incorporation of Si. Using localized vibration mode (LVM) spectroscopy, Manasreh et al (38) have seen that below a substrate temperature of 300°C there is a significant decrease in the amount of the incorporated Si that is substitutional. Man-
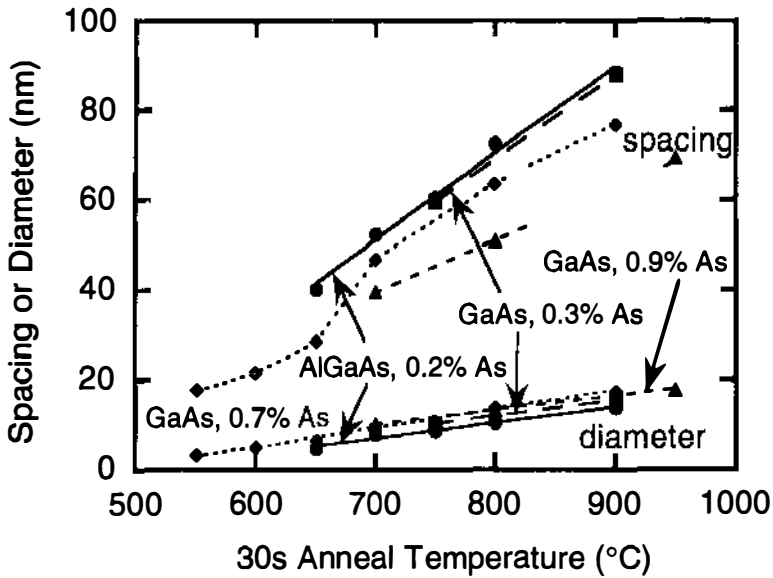
Figure 3 Density and average size of arsenic clusters in four different epilayers as a function of temperature for a 30 s anneal. Three of the epilayers are GaAs, one containing 0.3% excess arsenic, one containing 0.7% excess arsenic, and one with 0.9% excess arsenic. The fourth epilayer is AlGaAs containing 0.2% excess arsenic.

asreh et al (38) report a similar decrease in the incorporation of Be on substitutional sites for substrate temperatures below 300°C. However, McQuaid et al (39) found that almost all Si atoms were on Ga sites for a GaAs layer grown at 200°C with Si concentrations of 1×10^{19} cm^{-3}. The results of Manasreh and McQuaid indicate that the incorporation of Si on Ga sites at low substrate temperatures may be sensitive to the growth condition, i.e. group III-to-IV flux ratio, as has been observed by O'Hagan & Missous (40).

The effect of planes of dopants on the arsenic cluster coarsening was investigated by Melloch et al (14) and is illustrated with the TEM image in Figure 4. The white lines in the image are AlAs markers, the rest of the regions are GaAs. Planes of Si or Be dopants were incorporated into the epilayers at the positions indicated. These dopant planes were accomplished by interrupting growth by closing the shutter in front of the Ga effusion cell while maintaining the arsenic flux. The shutter in front of the Si (or Be) dopant effusion furnace was then opened to deposit the dopant to a sheet concentration of 5×10^{12} cm^{-2}. To make sure there was no effect of the growth interruption on the arsenic precipitation, the lower GaAs region in Figure 4 contained a growth interruption of the same
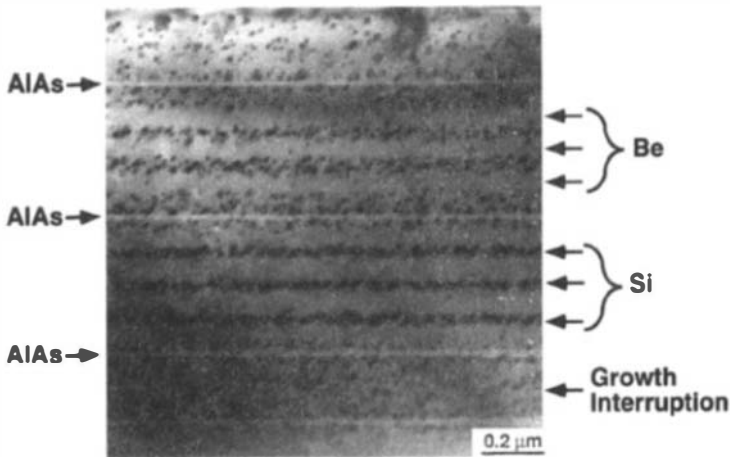
Figure 4   TEM image of a film structure grown at 250°C using As_2 and annealed for 30 s at 800°C. The white lines are 5 nm AlAs layers. Between the lower two AlAs layers is a 200-nm GaAs region that contained a 3-min growth interruption in the center. There is no apparent effect on the arsenic cluster coarsening due to the growth interruption. The next 400-nm region is a GaAs layer that contains three planes of Si dopants. The arsenic clusters are lined up on the planes of Si dopants. The next 400-nm region is a GaAs layer that contains three planes of Be dopants. The arsenic clusters are seen to coarsen preferentially between the planes of Be dopants.

duration (3 min) as used to deposit the planes of dopant atoms. After growth, the epilayer was annealed for 30 s at 800°C. Clearly seen in the figure is a preferential coarsening of the arsenic clusters at the planes of Si atoms, the *n*-type dopant, and away from the planes of Be atoms, the *p*-type dopant. The growth interruption had no effect on the arsenic cluster coarsening process. Cheng et al (41) have used this preferential coarsening of arsenic precipitates at Si delta-doped regions to demonstrate a GaAs/As superlattice.

To further investigate the effect of doping on the arsenic cluster coarsening process, Melloch et al (15) grew a *pn* doping superlattice where each doped region was 200-nm thick and doped to a concentration of 1×10^{18} cm^{-3}. Shown in Figure 5 is the TEM image of the epilayer after annealing to (*a*) 700°C and (*b*) 900°C for 30 s. With increased annealing there is a clear coarsening of the arsenic clusters and a preferential coarsening of the arsenic from the *p*-LTG-GaAs regions to the *n*-LTG-GaAs regions. Similar observations have been reported by Ibbetson et al (16). The behavior of the arsenic cluster--coarsening with doping is believed to be caused by the Schottky nature of the arsenic clusters (15). In *n*-GaAs: As, the arsenic clusters are negatively charged, whereas in *p*-GaAs: As they are positively
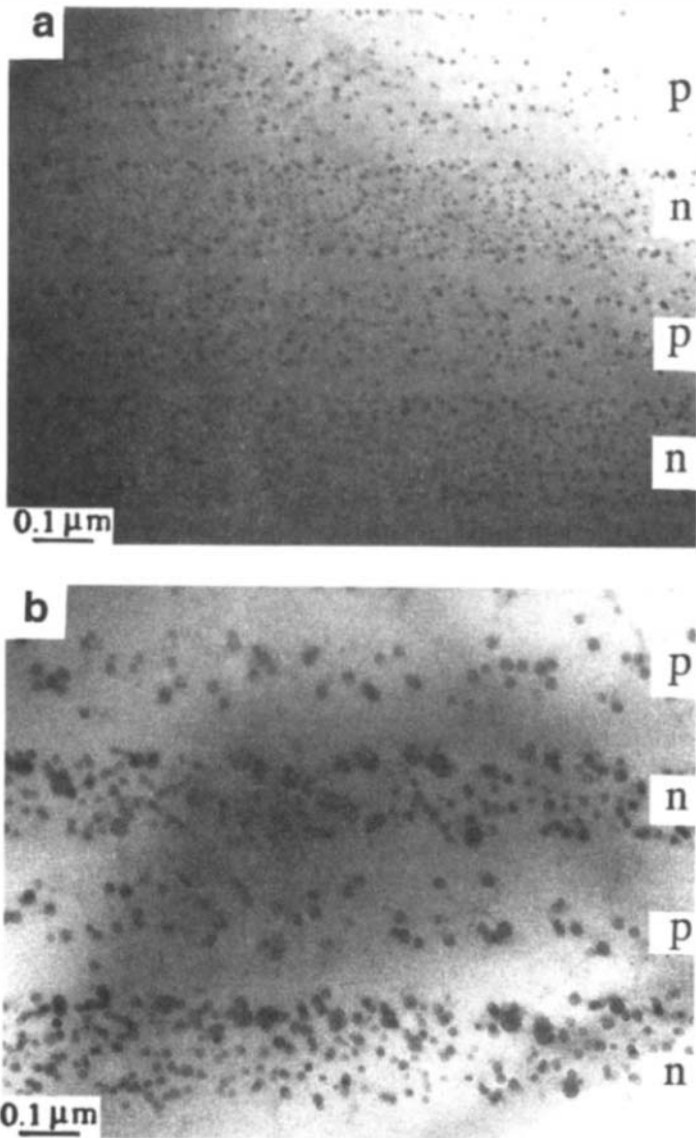
Figure 5   TEM image of a series of 200-nm GaAs regions uniformly doped with Si at 1×10^{18} cm^{-3} followed by a 200-nm GaAs region uniformly doped with Be at 1×10^{18} cm^{-3}, and subsequently annealed at (*a*) 700°C for 30 s and (*b*) 900°C for 30 s.

charged. Therefore, if an arsenic antisite or interstitial is thermally emitted from an arsenic cluster and is ionized, it will be positively charged and attracted to the arsenic cluster in n-GaAs: As but repelled from an arsenic cluster in p-GaAs: As. Thus the arsenic clusters will be more stable in n-GaAs: As than in p-GaAs: As and account for the preferential coarsening in n-doped regions.

Secondary ion mass spectroscopy (SIMS) of samples annealed at 800°C for 30 s and 950°C for 30 s are shown in Figure 6. There is no detectable diffusion of the dopants even for the 950°C 30 s anneal. In fact, SIMS characterization of a sample annealed for 10 min at 900°C also showed no discernible diffusion of the Be, unlike what is observed for Be in GaAs grown at normal (600°C) substrate temperatures. Apparently the excess arsenic in the film is preventing the Be from being interstitial, where it is a fast diffuser, and keeping it on substitutional sites, where it is a slow diffuser. Also seen in Figure 6 is the excess arsenic in the layers grown at 250°C (top 1.2 μm) compared to the underlying stoichiometric layers grown at 600°C. The variation in the arsenic concentration is clearly seen, with decreased concentrations in the regions corresponding to the p-n junction depletion regions, consistent with the TEM observations of Figure 5.

## Effect of Heterojunctions on Arsenic Cluster Formation

Mahalingam et al (13, 42) first noticed that if a heterojunction were present, the coarsening with anneal resulted in an accumulation of arsenic precipitates on the GaAs side of the heterojunction and a depletion of arsenic clusters on the AlGaAs side of the heterojunction. The behavior of the arsenic cluster formation and coarsening in a superlattice is illustrated in the TEM image of Figure 7. This is a TEM image of a series of 10-period $Al_{0.3}Ga_{0.7}As$/GaAs regions of progressively wider $Al_{0.3}Ga_{0.7}As$ barriers or GaAs wells, grown at low substrate temperatures and then annealed at 700°C for 30 s. For the wide GaAs wells, the arsenic clusters are completely contained within the GaAs well regions. As the well regions become narrower, the arsenic clusters are centered in the GaAs well regions but extend into the AlGaAs barrier regions. Finally the 10-period superlattice with the narrowest well and barrier widths is almost devoid of arsenic clusters, but the regions surrounding it (a GaAs region below and a superlattice above) contain arsenic clusters.

The behavior of the arsenic precipitate coarsening at heterojunctions and superlattices can be explained based on the difference in interfacial energies between an arsenic precipitate in GaAs and an arsenic precipitate in AlGaAs. Because the Al-As bond is stronger than the Ga-As bond, the interfacial energy will be lower between an arsenic precipitate and GaAs
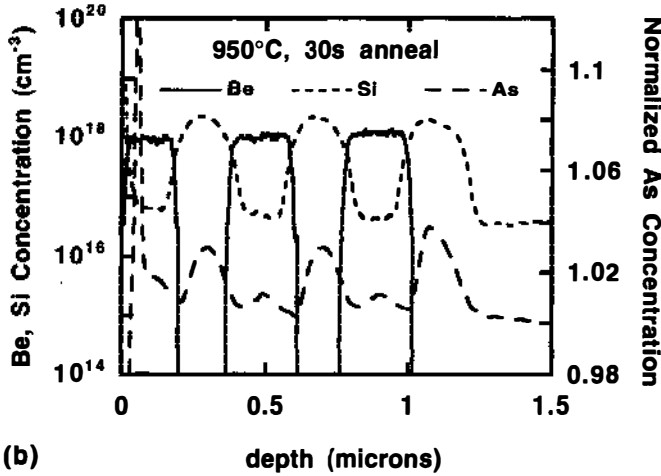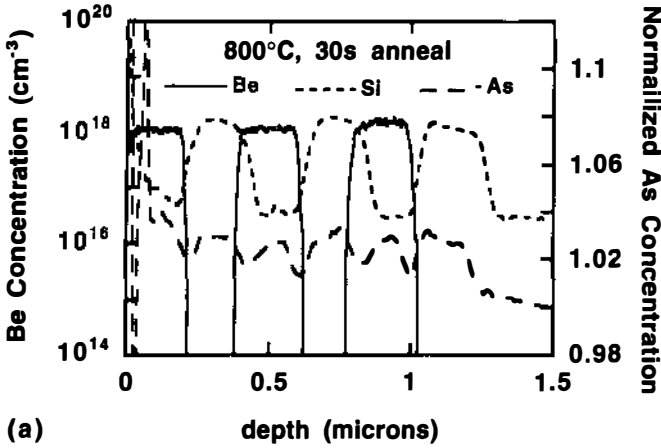
Figure 6   Secondary ion mass spectra of the doping superlattice after (*a*) 800°C 30 s annealing and (*b*) 950°C 30 s annealing. There is virtually no movement of the dopants, but the redistribution of the arsenic is evident. The arsenic concentration was normalized to its value in the film region grown at a substrate temperature of 600°C. Note that the Cs profiling of the Si gives much poorer depth resolution than the O profiling of the Be. This is why the Si profiles in the *n*-regions do not appear flat compared with the Be profiles in the *p*-regions.

than between an arsenic precipitate and AlGaAs. Therefore, the arsenic precipitates will preferentially coarsen from AlGaAs regions to GaAs regions. This is why the arsenic precipitates in the regions in Figure 7 with the thicker quantum wells are all contained in the quantum well regions. However, for the particular anneal condition used for the sample of Figure
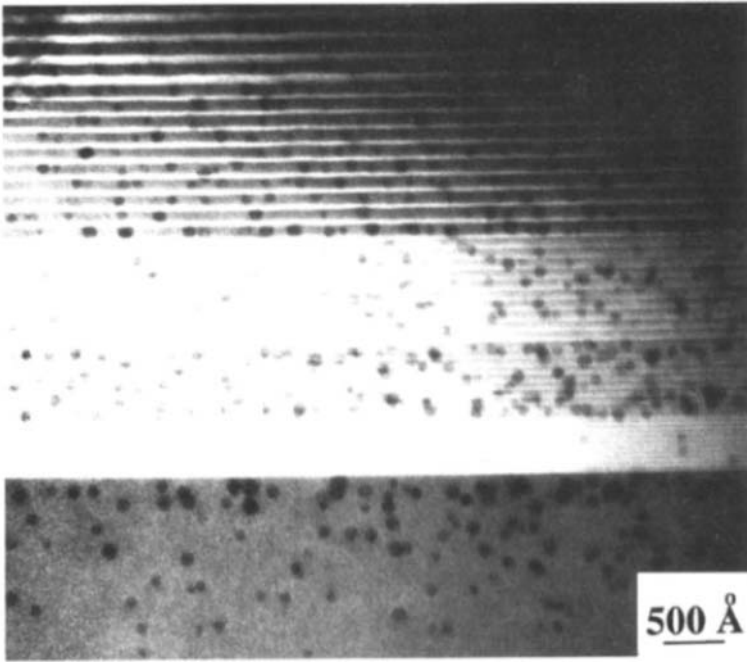
Figure 7   A series of 10-period superlattices of progressively wider $Al_{0.3}Ga_{0.7}As$ barriers or GaAs wells grown at low temperatures and then annealed at 700°C for 30 s.

7, in the thinner quantum well regions the arsenic precipitates are centered in the quantum wells but extend into the AlGaAs barriers because completely enclosing the arsenic precipitates in the quantum wells would require a larger number of smaller precipitates. This larger number of smaller precipitates would result in a larger arsenic precipitate-to-matrix interfacial area ratio and hence larger interfacial energy than fewer precipitates that are centered in the GaAs well regions that extend into the AlGaAs regions. Finally, the 10-period superlattice with the thinnest GaAs barriers is almost devoid of arsenic precipitates because it is thin compared with an arsenic diffusion length, and it is surrounded by regions of lower arsenic precipitate-to-matrix interfacial energies, i.e. the GaAs region below, and the 10-period superlattice above that has thicker GaAs well regions.

The behavior of the arsenic precipitates at AlGaAs/GaAs heterojunctions can be used to form planes of arsenic precipitates with high density. Shown in Figure 8 is the TEM image of a sample with 10-nm GaAs wells that are separated by 100-nm AlGaAs barriers. This structure was grown at low substrate temperatures so that excess arsenic was con-
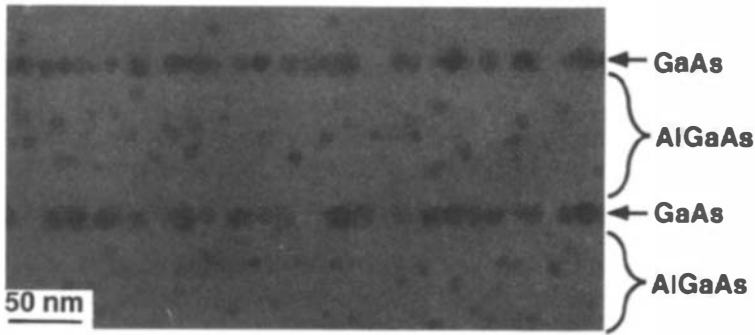
Figure 8 Bright-field image of 10-nm thick GaAs wells separated by 100-nm AlGaAs barriers for samples annealed at 700°C for 5 min.

tained throughout the GaAs and AlGaAs regions. The TEM image in Figure 8 is of a sample annealed at 700°C for 5 min. Even after the 5 min anneal at 700°C there is a clear tendency for the arsenic precipitates to coarsen to the GaAs well regions. After a 1.5 h anneal at 700°C there were very few arsenic clusters remaining in the AlGaAs regions (13). It may be possible to use this behavior of the arsenic precipitates at heterojunctions to get the arsenic precipitates close enough that they will behave as a buried conducting layer. Although the density of arsenic precipitates in Figure 8 appears high, the figure is a projection of a three-dimensional sample onto two dimensions. Therefore, the planes of arsenic precipitates in Figure 8 were not conducting—a higher density of arsenic precipitates is required than has been obtained so far. Similar behavior has been observed by Cheng et al (19) investigating precipitate coarsening in a structure consisting of InGaAs quantum wells and GaAs barriers. Cheng et al (19) observed preferential coarsening of the arsenic precipitates to the InGaAs quantum wells, the region of lower precipitate-to-matrix interfacial energy. Cheng et al (43) have also demonstrated preferential coarsening of arsenic precipitates at In delta-doped regions in GaAs and AlGaAs.

For engineering composite structures containing arsenic clusters, it would be desirable to be able to vary the placement of arsenic clusters between GaAs quantum wells and AlGaAs barrier regions. Melloch et al (44) have demonstrated such a capability. When growing at low substrate temperatures, a technique called migration enhanced epitaxy (MEE) can be used to grow highly stoichiometric epilayers (45). MEE consists of separately supplying about one monolayer of the group III and group V fluxes to the growing surface, which allows the excess arsenic to desorb from the surface. Therefore, by switching between MBE and MEE growth modes within a monolayer, one can change from stoichiometric to non-
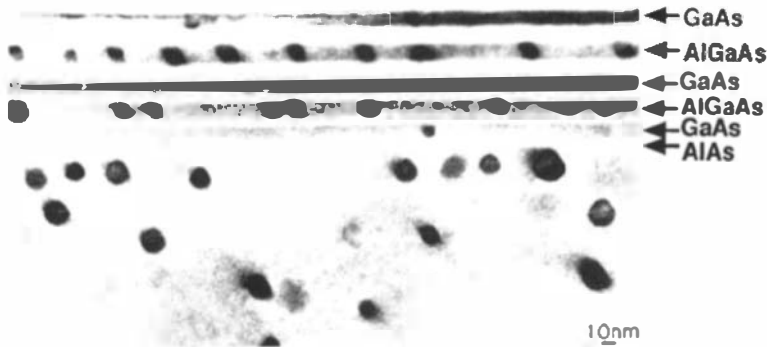
Figure 9   TEM image of a film structure grown at 260°C using As_4. The bright lines are AlAs layers (the lowest one is marked) and are either 6- or 12-nm thick. The region below the marked AlAs layer is the GaAs temperature transition region. The three GaAs wells in the image are indicated with arrows. The AlAs layers and the GaAs regions between the AlAs layers were grown by MEE, and as-grown are highly stoichiometric. The $Al_{0.2}Ga_{0.8}As$ layers were grown by MBE, and hence as-grown have a large excess of arsenic.

stoichiometric epitaxy. This technique then could allow one to grow GaAs wells that are stoichiometric and AlGaAs barriers that contain excess arsenic. However with annealing, the excess arsenic would still coarsen at the GaAs well regions. To prevent this, Melloch et al (44) used thin AlAs layers as arsenic diffusion barriers between the stoichiometric GaAs wells and the nonstoichiometric AlGaAs barriers to retain the excess arsenic and the arsenic precipitates in the AlGaAs barrier regions, as illustrated in Figure 9. The effectiveness of AlAs as a diffusion barrier to the large amount of excess arsenic in LTG-materials was first demonstrated by Yin et al (46).

Composite Formation Using Ion Implantation

Claverie et al (47) have demonstrated the fabrication of composites of arsenic clusters in GaAs by arsenic implantation and thermal annealing. Implantation allows lateral control of the placement of the excess arsenic with possible application for isolation between devices. With the use of implantation, one is not limited to arsenic as the only species introduced into the semiconductor. Chang et al (48) have formed Fe_3GaAs and Ni_3GaAs precipitates in GaAs using implantation of Fe and Ni followed with a precipitation anneal. The GaAs samples were implanted with

1×10^{16} ions/cm^2 of Fe or Ni at an energy of 170 keV and at room temperature. The samples were annealed at 950°C for 30 s or at 600°C for 30 min with a GaAs proximity cap. TEM analysis revealed a composite structure consisting of clusters in the GaAs matrix. The size of a typical precipitate was 35 nm in diameter, with moiré fringes clearly visible. Microdiffraction experiments showed the presence of extra spots in the diffraction pattern, which were attributed to the presence of hexagonal Fe_3GaAs or Ni_3GaAs in a particular orientation with respect to the GaAs matrix. The (004) X-ray rocking curves of the annealed samples showed only a sharp substrate peak and no extra peak as observed before annealing. This indicates that most of the strain in the matrix is relaxed by precipitation. The optical properties of these new composites are yet to be explored. Preliminary Hall-effect measurements on the Fe- and Ni-implanted samples that were annealed at 950°C for 30 s showed they are both p-type, with carrier concentrations of 2.5×10^{17} cm^{-3} and 7.5×10^{17} cm^{-3}, with mobilities of 179 and 252 cm^2/V-s, respectively. This large hole concentration is probably due to residual Fe and Ni atoms that act as acceptors. The ability to form these composites with different metals may allow an additional degree of control of the composite properties because of the different Schottky barriers associated with different metal/GaAs interfaces. Precipitates of noble metals such as Cu and Ag in GaAs produce particularly strong absorption and scattering of optical radiation and may represent attractive new composite materials for optical applications (49).

ROLE OF POINT DEFECTS AND ARSENIC CLUSTERS

Electrical Conductivity

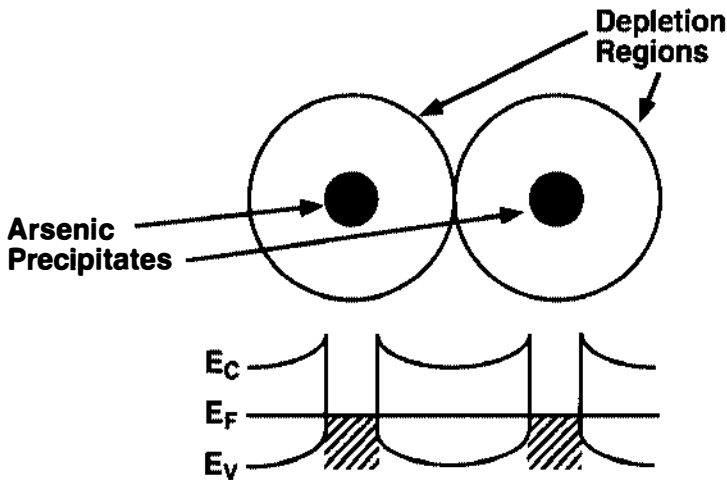In LTG-GaAs much of the excess arsenic, with concentrations of 1 to 2%, can be in the form of the arsenic antisite (As_{Ga}), the arsenic interstitial (As_i), the Ga vacancy (V_{Ga}), and complexes of these defects. The observation of the ionized arsenic antisite ($As_{Ga}+$) with concentrations of up to 1 to 5×10^{18} cm^{-3} in LTG-GaAs was made using electron paramagnetic resonance (EPR) (7). This concentration of $As_{Ga}+$ is equal to the concentration of ionized acceptors, presumably the ionized Ga vacancy ($V_{Ga}-$). The observation of the neutral As_{Ga} has been made using absorption measurements (50, 51). Because of the large concentration of point defects, LTG-GaAs exhibits hopping conductivity with resistivities as low as 10 Ω-cm (52). However, with annealing, the resistivity increases dramatically to as high as 10^6 Ω-cm for annealed LTG-GaAs (52), and resistivities as high as 6×10^{11} Ω-cm have been reported for annealed LTG-$Al_{0.3}Ga_{0.7}As$ (53). For intermediate growth temperature, 350–450°C, as-

grown GaAs is semi-insulating (10^7 Ω-cm) due to the incorporated point defects (4, 54).
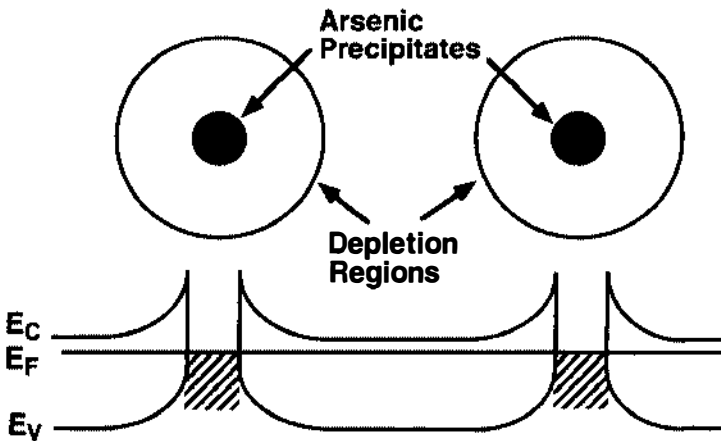
There has been considerable debate concerning the role of point defects vs the role of arsenic precipitates in explaining the electrical properties displayed after annealing LTG-materials (21, 52, 55, 56). The defect model predicts a decrease in hopping conductivity as the excess arsenic precipitates but assumes that the arsenic precipitates play little role and that the material is compensated by the residual arsenic antisites. The model based on arsenic precipitates as embedded Schottky contacts assumes a depletion region around each arsenic precipitate. If the background doping is low enough, compared with the spacing of the precipitates, the material will be completely depleted, as illustrated in Figure 10a, and will exhibit a high resistivity. The degree to which the defects or the embedded Schottky barriers control the material properties depends on the anneal that the material has experienced. The transition from a material dominated by point defects to one dominated by the arsenic precipitates occurs around 600°C—the only anneal temperature or the maximum anneal temperature used in much of the data reported in the literature.

The conductivity as a function of anneal temperature of LTG-GaAs has been reported by Ibbetson et al (23). They found that the room-temperature conductivity of an LTG-GaAs sample annealed for 30 s at 600°C was due to hopping conduction. For higher-temperature anneals, the room-temperature conductivity was not the result of hopping conduction but due to a thermally assisted tunneling process with an activation energy of ~ 0.6 eV, which Ibbetson et al attribute to the arsenic precipitates. In fact, this activation energy of ~ 0.6 eV is very close to the reported Schottky barrier height for arsenic deposited on GaAs (57).

Atique et al (58) have studied the structural and electronic properties of doped LTG-GaAs as a function of anneal for three 1 μm-thick epilayers with Si doping concentrations ranging from 5×10^{17} cm^{-3} to 5×10^{18} cm^{-3} and five 1 μm-thick epilayers with Be doping concentrations ranging from 5×10^{17} cm^{-3} to 5×10^{19} cm^{-3}. These epilayers were all grown under similar conditions; the Si-doped epilayers contained 0.9% excess arsenic, and the Be-doped epilayers contained 0.6% excess arsenic. The epilayers were grown on semi-insulating GaAs substrates; after epitaxy, each wafer was cleaved into a series of samples. Samples from the Si-doped epilayers were annealed for 30 s at temperatures ranging from 650 to 1000°C, and samples from the Be-doped epilayer were annealed at temperatures ranging from 650 to 900°C. Van der Pauw structures were fabricated on the samples to ascertain the electrical properties. Shown in Figure 11 are the resistivities of these samples as a function of anneal temperature. The 30 s anneal at 700°C results in a significant increase in resistivity of the samples (limited

Depletion
Regions

Arsenic
Precipitates

E_C
E_F
E_V

(a)

Arsenic
Precipitates

Depletion
Regions

E_C
E_F
E_V

(b)

Figure 10 (*a*) Depletion regions around arsenic precipitates such that the depletion regions just overlap. (*b*) Depletion regions around arsenic precipitates with spacing such that there is undepleted material between the precipitates.

by substrate conduction) from the as-grown values, except for the most heavily doped Si sample. The resistivity is seen to decrease as the anneal temperature is raised above 700°C because of arsenic cluster coarsening, which causes the depletion regions around the arsenic clusters to no longer
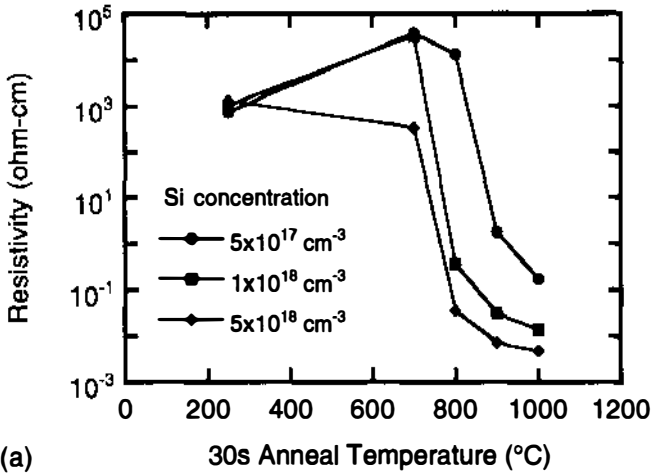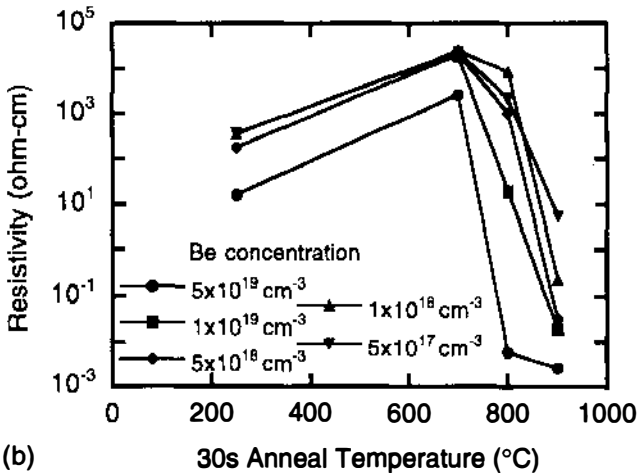
Figure 11 Resistivity as a function of temperature for 30-s isochronal annealing of GaAs
epilayers containing excess arsenic for (a) three different n-type doping concentrations, and
(b) five different p-type doping concentrations.

overlap, as illustrated in Figure 10b. This effect is clearly seen in the carrier
concentrations (as determined by Hall measurements) as a function of
anneal temperature for these epilayers (Figure 12). Also of note is that
some of the p-doped epilayers are n-type as-grown or when annealed at
low temperature, as has been observed by others (40, 59). The mobilities
as a function of anneal for the n-GaAs:As samples are shown in Figure
13.
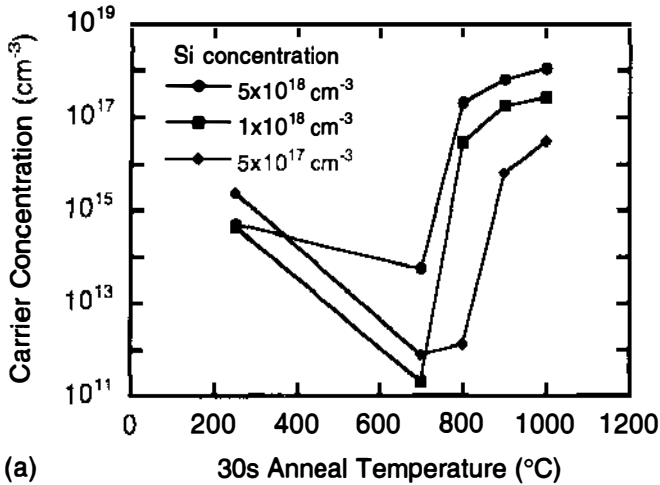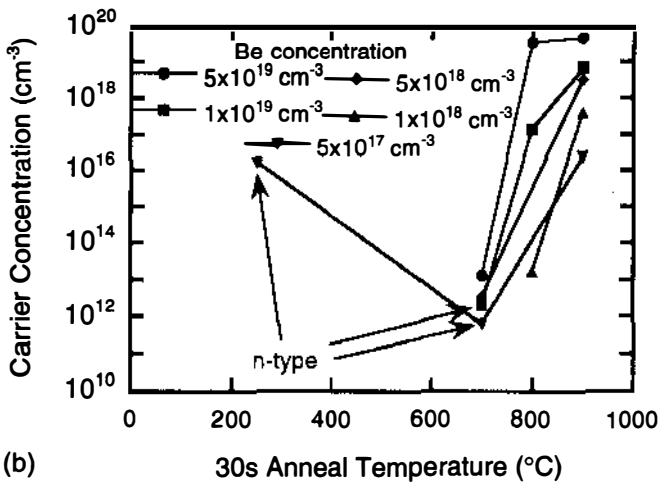
Figure 12 Carrier concentration as a function of temperature for 30-s isochronal annealing of GaAs epilayers containing excess arsenic for (*a*) three different *n*-type doping concentrations and (*b*) five different *p*-type doping concentrations.

Atique et al (58) have investigated the correlation between the measured carrier concentrations and the average arsenic precipitate size and average arsenic precipitate spacing. Figure 14 shows the model and band structure of an arsenic precipitate surrounded by its spherical depletion region. In this model, the arsenic precipitate forms a Schottky barrier with the GaAs matrix analogous to a planar Schottky barrier. By solving Poisson's equa-

Figure 13 graph with y-axis "Mobility (cm²/Vs)" ranging 0 to 2000, x-axis "30s Anneal Temperature (°C)" from 0 to 1200. Legend: 5x10^18 cm^-3, 1x10^18 cm^-3, 5x10^17 cm^-3.
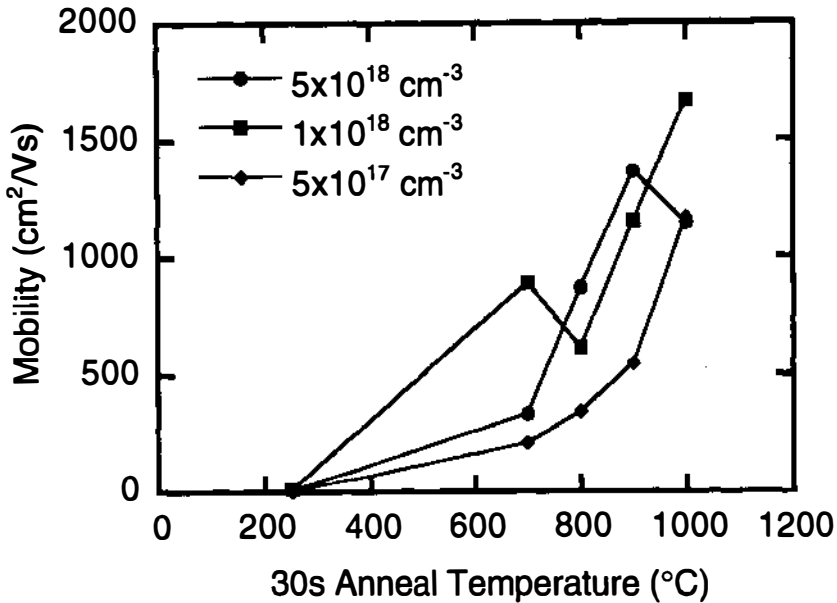
Figure 13 Mobility as a function of anneal temperature for 30-s isochronal anneals for the Si-doped LTG-GaAs epilayers.

tion, the built-in potential V_o in Figure 14—determined from the doping level of the material—is related to the arsenic precipitate radius r_o and the depletion radius r_s by (21)

$$V_o = -(qN_D/6\varepsilon)[(2r_s^3/r_o) + r_o^2 - 3r_s^2],$$ 1.

where N_D is the doping density, and ε is the permittivity of the semi-conductor matrix. This equation allows the calculation of the depletion radius for each of our samples, which enables an estimation of the free carrier concentration from the fraction of material depleted. The expected free carrier concentration N_f for each sample is related to the doping density N_D, the depletion radius r_s, and the distance between precipitates d by

$$N_f = N_D[1 - (2r_s/d)^3].$$ 2.

Atique et al (58) define $2r_s/d$ as the degree of depletion. (A degree of depletion of 1 occurs when the depletion regions just touch, and a degree of depletion of 1/2 is the case when the depletion regions extend to include half the distance between precipitates.) Plotted in Figure 15a,b are the free electron and free hole carrier concentrations determined from Hall measurements vs the degree of depletion as determined from TEM
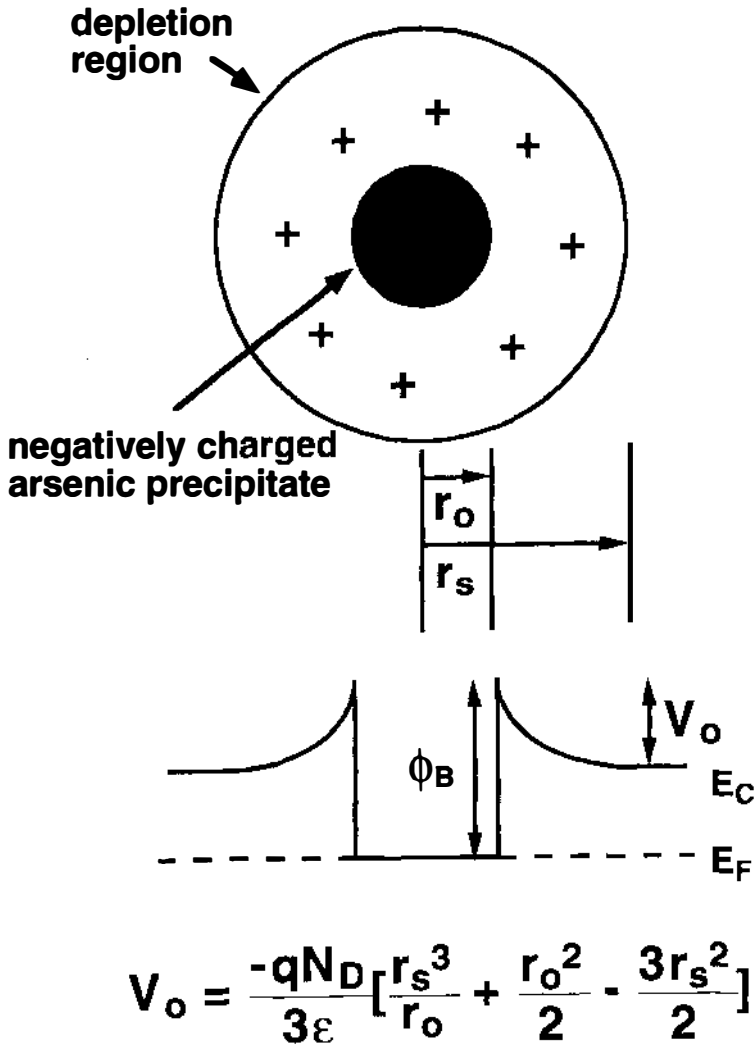
depletion region

negatively charged arsenic precipitate

r_o

r_s

ϕ_B

V_o

E_C

E_F

$$V_o = \frac{-qN_D}{3\varepsilon}\left[\frac{r_s^3}{r_o} + \frac{r_o^2}{2} - \frac{3r_s^2}{2}\right]$$

Figure 14   Schottky barrier model for the embedded arsenic precipitates.

measurements. Also plotted in Figure 15 is Equation 2, the expected free carrier concentration based on the arsenic clusters acting as internal Schottky diodes. The measured free electron concentration data correlate well with the model of the arsenic clusters acting as internal Schottky barriers. Note that any residual AsGa defects, As_{Ga} deep donors, would not be able to decrease the free electron densities. In Figure 15b, as the Be concentration increases, the drop in the free hole concentration is seen to
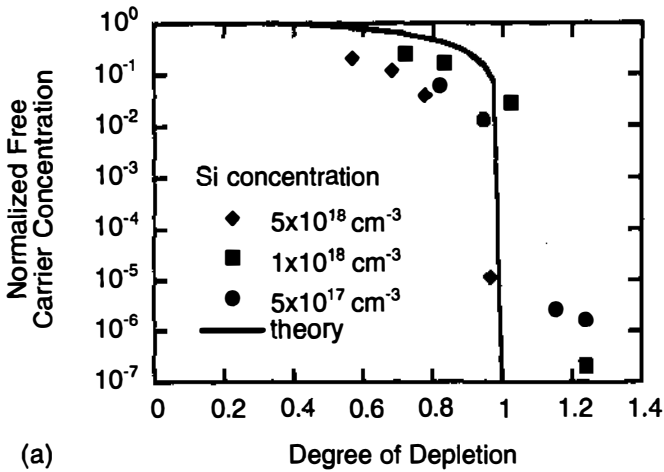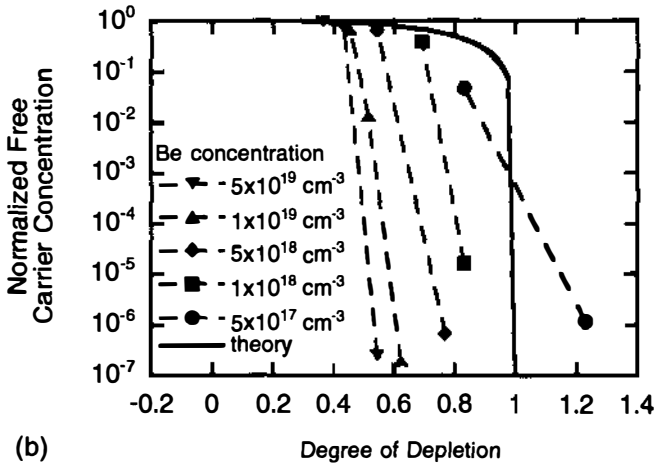
Figure 15 Normalized carrier concentration vs degree of depletion for (*a*) three different Si-doping levels and (*b*) five different Be-doping levels. Degree of depletion is $2 r_s/d$, where r_s is the depletion sphere radius and d is the distance between precipitates.

occur at lower values of degree of depletion, or arsenic cluster spacing, than expected from the internal Schottky barrier model. This is attributed to As_{Ga} partially compensating the shallow Be acceptors. For a given anneal condition, the concentration of As_{Ga} will be higher in *p*-doped LTG-GaAs than in *n*-doped LTG-GaAs because there is less of a driving force for precipitation because of the locations of the Fermi levels (15). In LTG-*p*-GaAs, the As_{Ga} will compensate the shallow acceptors, thus the Fermi level begins at midgap. In LTG-*n*-GaAs, the As_{Ga} defects do not

compensate the shallow Si donors, thus precipitation of the excess arsenic is required to move the Fermi level to midgap.

The average arsenic cluster size and spacing as a function of anneal is shown in Figure 16a for the Si-doped epilayers and in Figure 16b for the Be-doped epilayers, illustrating the coarsening of the arsenic clusters with annealing. Note that as the doping density increases for a given anneal condition, the average diameter and spacings of the arsenic clusters are smaller. The reason for this trend is that for higher doping densities at a
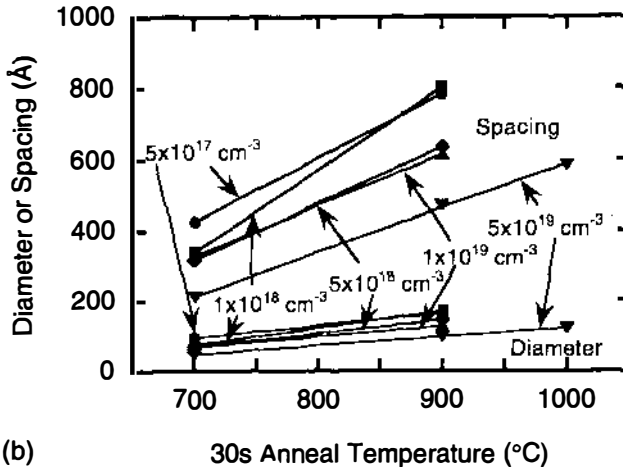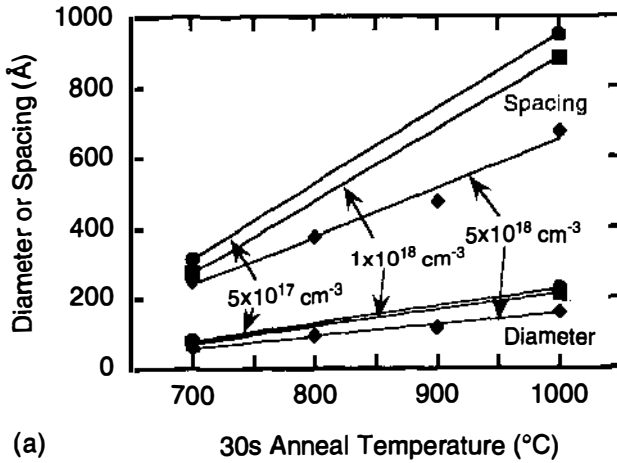
Figure 16 Average cluster sizes and spacings as a function of anneal temperature for 30-s isochronal annealing of LTG-GaAs epilayers for (a) three different Si-doping levels and (b) five different Be-doping levels.

given anneal condition, a smaller spacing between precipitates is required to move the Fermi level toward midgap—toward a state of lower free energy.

Fermi Level Position

Several groups have made effective use of the contactless electro-modulation methods of photoreflectance (60) and contactless electro-reflectance (60) to study the nature of Fermi level pinning on LTG-GaAs and GaAs:As (56, 61–65) and InGaAs:As (66). Certain features, i.e. Franz-Keldysh oscillations, observed in electromodulation from special structures with large, uniform electric fields have been found to be extremely useful for evaluating Fermi-level positions (60). Although the work of Warren et al (56, 61, 62) was carried out on both n- and p-type material, the investigations of References 63–65 were performed on only n-type samples. In addition, Warren et al (56, 61, 62) used piezoreflectance to further evaluate the nature of the electric fields created by the Fermi-level pinning. The experiments of Warren et al showed that the Fermi level in LTG-p-GaAs is pinned 0.4 eV below the conduction band edge, whereas in p-GaAs:As the Fermi level is pinned 0.67 eV below the conduction band edge, i.e. midgap. In addition, these experiments of Warren et al showed that the Fermi level is unpinned in LTG-n-GaAs and pinned at midgap in n-GaAs:As. Thus the controlling mechanism in the GaAs:As material is indeed that of Schottky barrier-controlled pinning on metallic arsenic precipitates, consistent with previously reported investigations for these materials.

To probe the electric fields in and adjacent to the LTG layers, special three-layer heterostructure stacks were grown for the electromodulation measurements. They consisted of a doped/undoped (layer I)/undoped (layer II) configuration, where undoped layer I is either GaAs or InGaAs grown at normal MBE substrate temperatures, and undoped layer II is either LTG-GaAs, GaAs:As, or InGaAs:As. In the work of Warren et al (56, 61, 62), the structures were n^+ (N) and p^+ (P) GaAs buffer layers (doped at 5×10^{18} cm^{-3}) grown on (001) substrates, followed by 50-nm undoped (U) GaAs grown at a substrate temperature of 600°C. The substrate temperature was then dropped to 250°C, and 150 nm of GaAs was deposited for samples referred to as LTUN and LTUP, respectively. In other samples, this recipe was followed by an in situ ramp back up to 600°C for a 30 s anneal in an As$_2$ flux. These samples are referred to as ALTUN and ALTUP layers. The key assumption in using this method with the three-layer structure is that the Fermi level will be pinned at some characteristic energy in layer II. If so, the electric field will be (a) nearly zero in layer II and (b) nonzero and nearly constant in undoped layer I. A

knowledge of the thickness of undoped layer I and the doping level of the buffer layer makes it possible to evaluate the Fermi level in layer II. Electric fields in the undoped regions of all these samples were then measured from the Franz-Keldysh oscillations observed, using both photoreflectance and contactless electroreflectance. These two techniques gave identical fields; in addition, contactless electroreflectance gave the field sign from the phase of the reflected signal (60). There were no observable photovoltage effects in the ALTUN and ALTUP materials at 300 K. In the LTUN and LTUP samples, measurements were made at elevated temperatures (~ 400 K) to eliminate the influence of the photovoltage (60).

It is important to note that recent experiments have demonstrated the need to study both n- and p-type material to obtain unambiguous results about Fermi-level positions (67). In addition to the above studies, Warren et al also have performed piezoreflectance measurements at 300 K on all samples to determine the nature of the fields (i.e. uniform or nonuniform) responsible for the Franz-Keldysh oscillations. It has been demonstrated that only uniform fields produce Franz-Keldysh oscillations in piezoreflectance spectra (60).

In the LTUN structure, the measured field from the Franz-Keldysh oscillations in the electromodulation traces was 1.1×10^5 V/cm, which corresponds to the built-in field at the U-N interface. For this sample, no Franz-Keldysh oscillations were observed in piezoreflectance, indicating that the field is nonuniform. This value places an upper limit of about 0.5 eV for the Fermi-level distance from the conduction band edge at the LT-U interface. In the LTUP sample, the measured field from electromodulation was 1.8×10^5 V/cm, which corresponds to a Fermi-level position in the LT material ~ 0.45–0.5 eV below the conduction band. The uniform nature of this field was verified by the Franz-Keldysh oscillations in the piezoreflectance data, which also gave the same value of the field as the electromodulation measurement. These two measurements are exactly what one would expect from a single, deep-donor level 0.4 eV below the conduction band, which corresponds to the EPR and infrared absorption measurement of arsenic-antisite defects (7, 50, 51). Figure 17a,b shows our modeling results for the LTUN and LTUP cases, respectively, with such a defect, illustrating the lack of firm pinning for this system. This model also serves to explain the presence of a photovoltaic effect in these samples. These figures are consistent with the piezoreflectance data, i.e. nonuniform field (1.1×10^5 V/cm) in the U region near the U-N interface for the LTUN sample and uniform field (1.8×10^5 V/cm) in the U region for the LTUP material.

Data from the ALTUN and ALTUP samples, however, indicate a completely different system. Shown in Figures 18 and 19 are the contactless
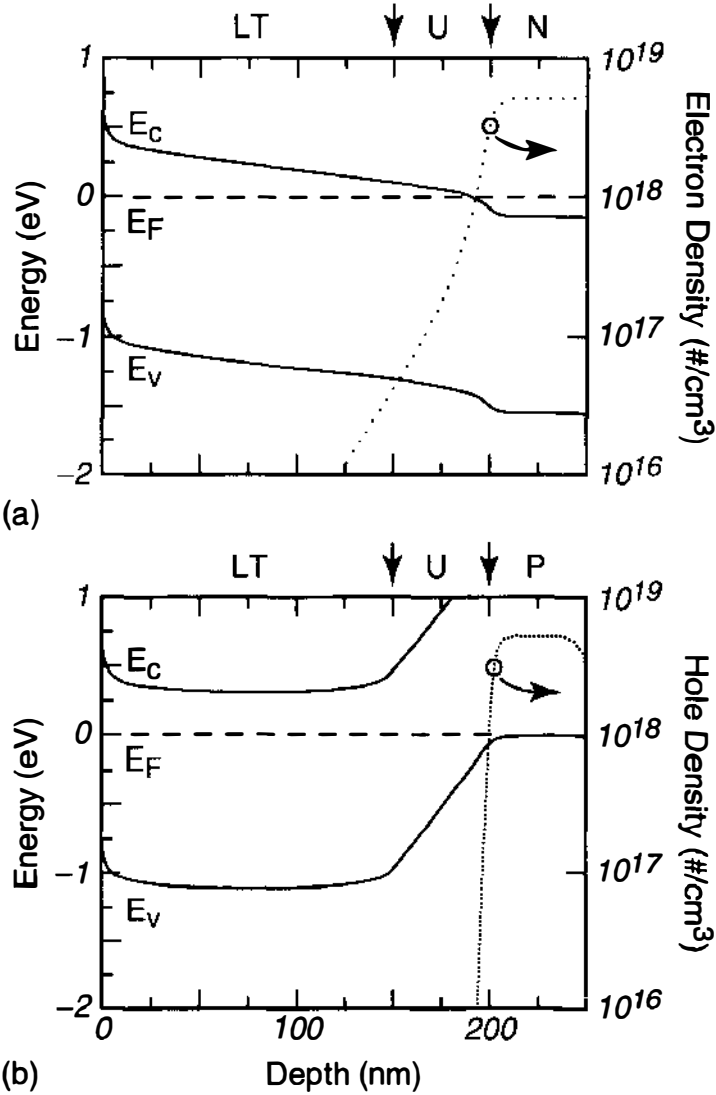
Deep Donor: $E_D = E_c - 0.4$ eV, 10^{19} cm^{-3}

Figure 17   Band profile for the as-grown (un-annealed) (*a*) LTUN and (*b*) LTUP structures. A deep donor is included in the LT material with energy 0.4 eV below the conduction band. Arrows indicate the interface between the LT, U, and N layers.
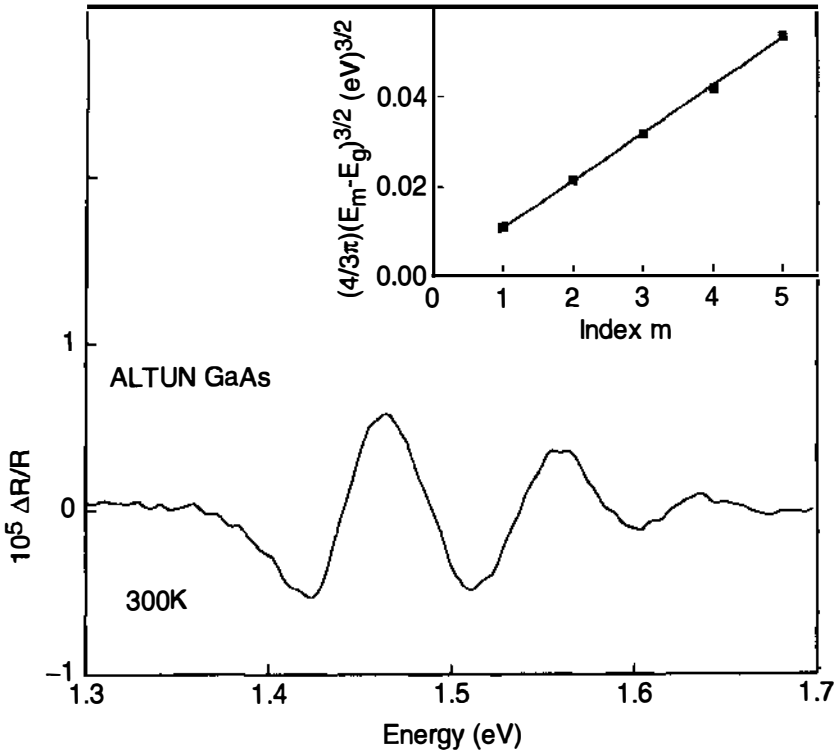
Figure 18 Contactless electroreflectance spectrum from the ALTUN structure at 300 K. The inset shows a plot of $(4/3\pi)(E_m-E_g)^{3/2}$ as a function of the Franz-Keldysh oscillations extrema index m.

electroreflectance spectra at 300 K for these two samples, respectively. Both samples display a number of Franz-Keldysh oscillations, although the signals exhibit opposite phases consistent with n- and p-type band bending, respectively. Also the piezoreflectance traces from both materials exhibited Franz-Keldysh oscillations, indicating linear electric fields. The positions of the mth extrema in the Franz-Keldysh oscillations are given by (60)

$$m\pi = (4/3)[(2\mu_\parallel)^{1/2}(E_m - E_g)^{3/2}/q\hbar F] + \chi, \qquad 3.$$

where E_m is the photon energy of the mth extrema, E_g is the band gap, F is the electric field, $\mu_\parallel$ is the reduced interband effective mass in the direction of $\vec{F}$ and χ is an arbitrary phase factor. Therefore, if $\mu_\parallel$ is known, a plot of $(4/3\pi)(E_m-E_g)^{3/2}$ as a function of index number m yields a straight line from which F can be evaluated from Equation 3. In the case of the uniform electric fields in these structures, the relation between F and the barrier height (V_B) created by the Fermi-level pinning can be written as (60)
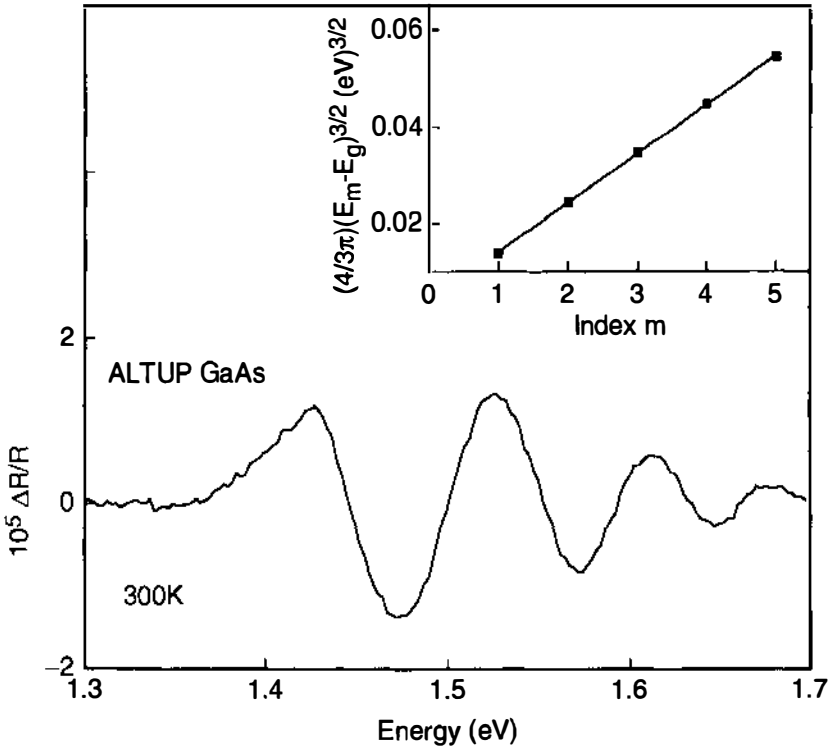
Figure 19 Contactless electroreflectance spectrum from the ALTUP structure at 300 K. The inset shows a plot of $(4/3\pi)(E_m-E_g)^{3/2}$ as a function of the Franz-Keldysh oscillations extrema index m.

$$V_B = FL + (kT/q) + SCC, \qquad\qquad 4.$$

where L is the thickness of undoped layer I and the second and third terms are the Debye length and space charge (doping layer) corrections, respectively.

The insets of Figures 18 and 19 display such plots from which the authors have deduced fields of 1.25×10^5 V/cm for both samples, which indicate a single midgap GaAs : As Fermi-level position for both materials. Modeling for the ALTUN and ALTUP structures are shown in Figure 20a,b, respectively. Allowing for doping degeneracy and Debye tailing in the doping substrates, and an 8-nm Debye tail in the GaAs: As layer, their calculations yield fields of 1.3×10^5 V/cm with a pinning of 0.67 eV below the conduction band edge. The extrapolated pinning position is in excellent agreement with a measured Fowler-Nordheim photoresponse threshold of 0.7 eV (25) and is what one would expect from the barrier height of
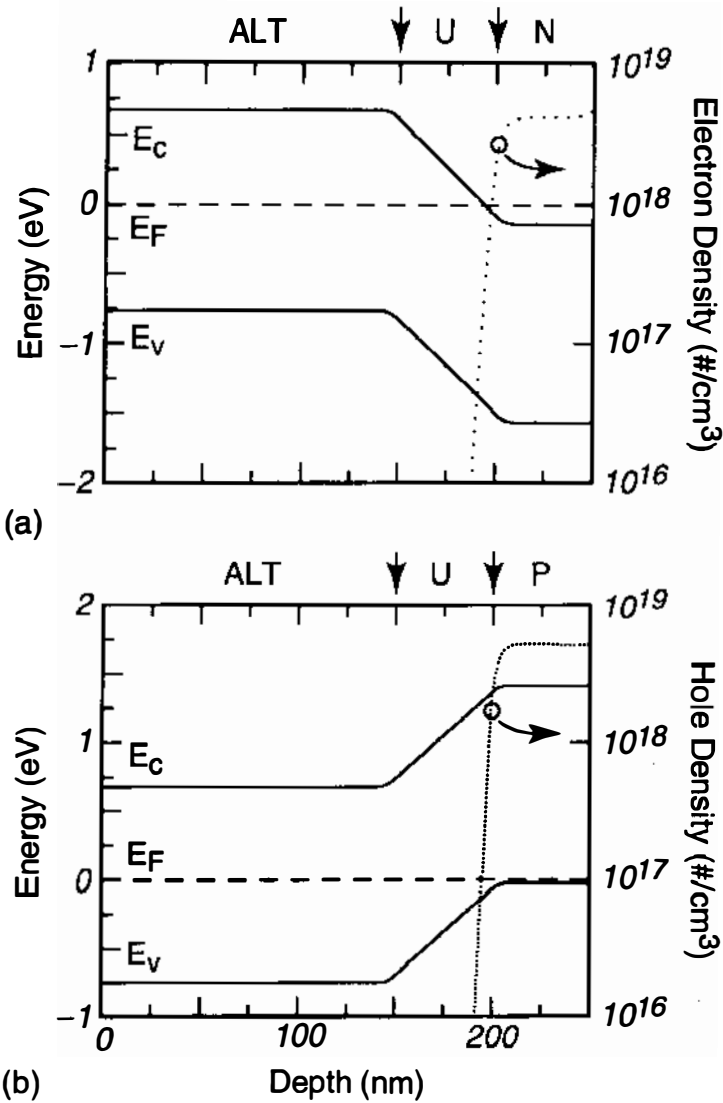
PINNED: $E_F = E_C - 0.7$ eV

Figure 20   Band profile for the annealed (*a*) ALTUN and (*b*) ALTUP structures. The Fermi level is pinned at 0.67 eV below the conduction band edge. Arrows indicate the interface between the LT, U, and N layers.

metallic arsenic to GaAs (57). The fact that there was no measurable photovoltage in these samples is consistent with metallic Fermi-level pinning by the arsenic precipitates. In addition, it is clear that such pinning could not be produced by a single donor or acceptor defect.

Woodall et al also have reported a similar experiment on two ALTUP (sample A and B) and one UP (sample C) GaInAs/InP (001) samples (66). Samples A and B were three-layer structures—the doped layer was p-type GaInAs, the undoped layer I was GaInAs 100-nm thick, and the undoped layer II was GaInAs:As 100-nm thick. Sample C is the same as samples A and B but without the GaInAs:As layer II. For sample C, the Franz-Keldysh oscillations measure the pinning position of the free surface of GaInAs. The photoreflectance spectra at 300 K for these three samples are shown in Figure 21. All three materials exhibit well-pronounced Franz-Keldysh oscillations. For clarity, the spectra are plotted in terms of $E-E_g$. The values of E_g listed in the figure were obtained from the three-point method. The electric fields were 46 ± 3, 44 ± 3, and 50 ± 3 kV/cm, from which the authors deduced Fermi levels of 0.49 ± 0.03 V, 0.47 ± 0.03 V, and 0.53 ± 0.03 V above the valence band edge for samples A, B, and C, respectively. If the GaInAs:As did not pin the Fermi level, then because
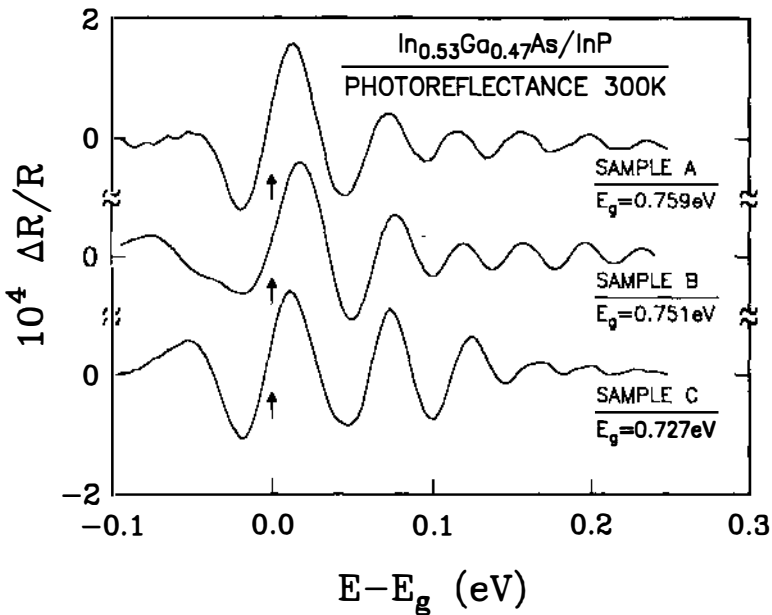
Figure 21   Photoreflectance spectra at 300 K for two ALTUN (samples A and B) and one UP (sample C) GaInAs/In/InP materials plotted as a function of ($E-E_g$).

of the differences in undoped GaInAs thickness between the samples A, B and sample C, the electric fields in samples A and B would have to be about one half the value of sample C in order for the Fermi levels at the surface to be the same for all three materials. This is clearly not the case. Thus this study demonstrated that the Fermi level is pinned at about the same value for both GaInAs surfaces and GaInAs : As.

Scanning Tunneling Microscopy Studies

Feenstra et al (27, 68–70) have used scanning tunneling microscopy (STM) to investigate LTG-material as it changes with annealing from one with a distribution of point defects to one with a distribution of arsenic clusters. An STM image of as-grown material is shown in Figure 22, revealing a concentration of arsenic antisites of about 1×10^{20} cm^{-3} (68, 69). The characteristic appearance of the antisites in the STM images arises from
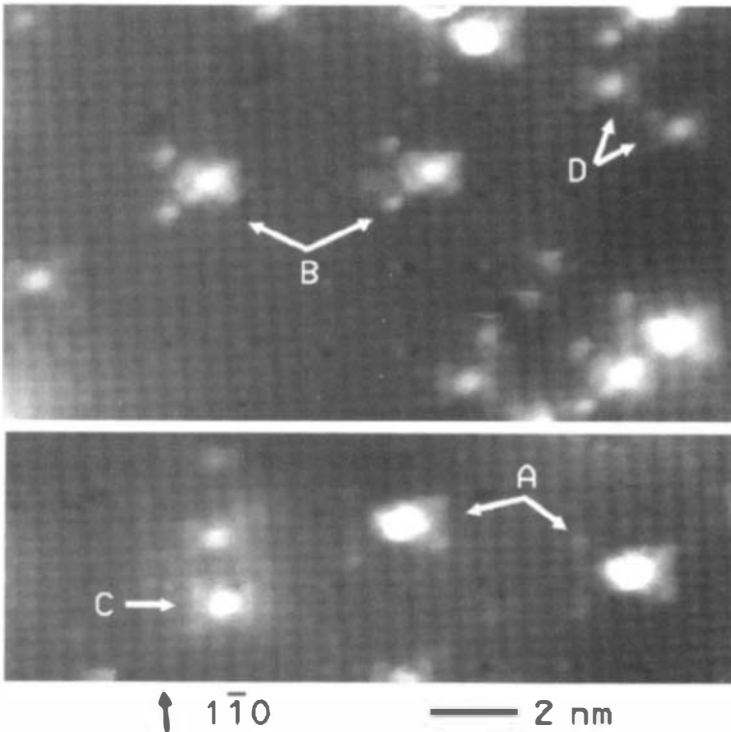
Figure 22   STM images of the (110) cleaved surface of as-grown LTG-GaAs, acquired with 0.1 nA tunnel current and at a sample voltage of -2.0 V. Various point defects can be seen, classified as types A, B, C, and D, as indicated.

the wave function of the defect donor states, and the labels A, B, C, D in Figure 22 refer to antisites located in crystal planes located 0, 1, 2, or 3 planes respectively below the (110) surface. Tunneling spectroscopy directly reveals the spectrum of midgap donor states ($0/+$ and $+/++$), as shown in Figure 23. As the background doping of the material changes from n-type to p-type, the Fermi level moves into the middle of this band
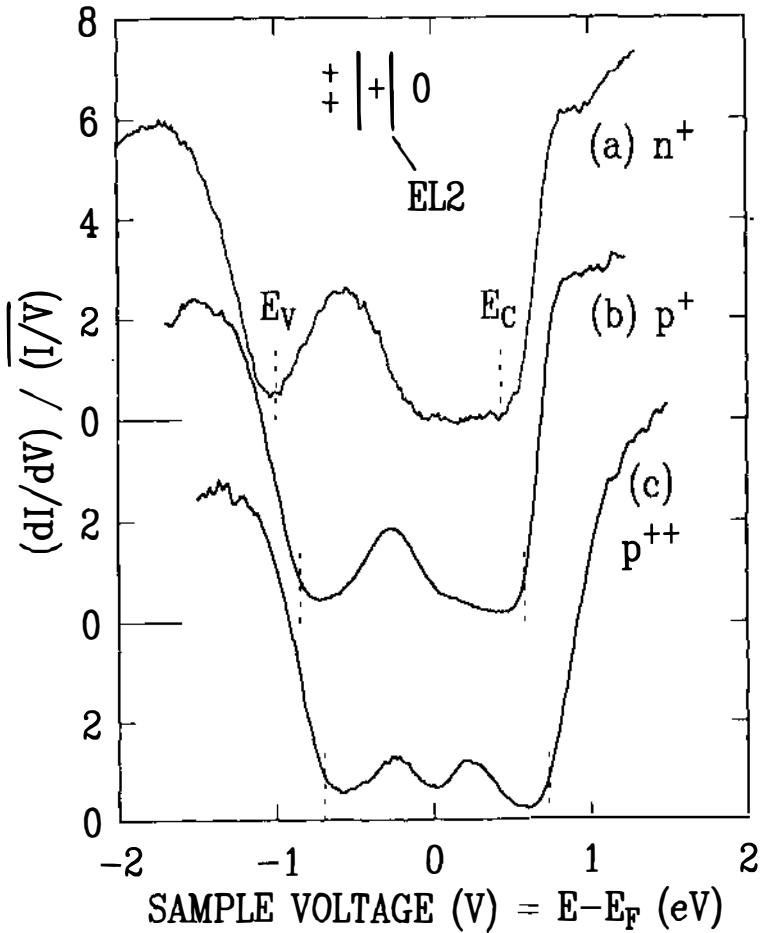

Figure 23 Tunneling spectra acquired from layers of as-grown LTG-GaAs containing varying amount of compensating shallow dopants. The valence-band maximum E_V and conduction-band minimum E_C are indicated by dashed lines in each spectrum. An intense band of states, arising from arsenic-related defects, appears within the band gap. The states of a bulk arsenic antisite defect (EL2) are shown in the upper part of the figure, relative to the band edges of spectrum (*a*).

of donor states. A local minimum in conductance forms at the Fermi level and is attributed to Coulomb interactions (both on-site and off-site) at the defects (68, 69).

STM studies of annealed material are shown in Figures 24–29. In all cases, the structures studied consist of a layer of LTG-GaAs with thickness of 500 to 1500 Å, surrounded on both sides by highly doped GaAs layers grown at temperatures near 600°C. Figure 24 is obtained from n-type LTG-material doped at 1×10^{19} cm^{-3}, with a 30 min anneal at 600°C (27). Arsenic clusters appear there as either protrusions or depressions in the LTG annealed (denoted LTA) layer, with typical diameter of 50 Å. The density of these features is found to be 1.2×10^{17} cm^{-3}, in reasonable
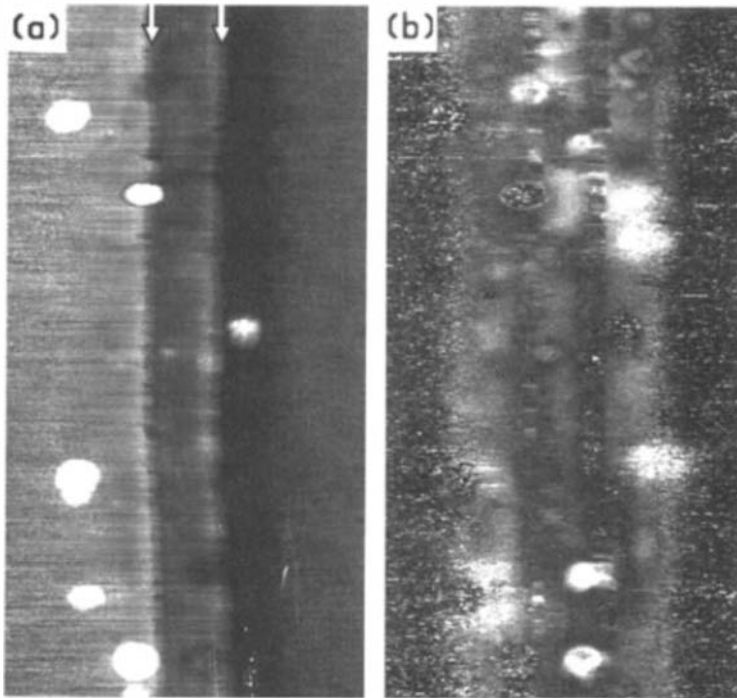
Figure 24   STM image of a cleaved GaAs structure, showing (*a*) topography and (*b*) conductance, acquired at a sample voltage of -2.5 V. The gray-scale range in (*a*) is 8 Å. As indicated in (*b*), the structure contains an LTA n-type layer, surrounded by p-type layers grown at higher temperature. The sample was annealed at 600°C. Two steps occur in the LTA-layer, as marked by arrows in (*a*).

agreement with that found in TEM studies (56). Antisite defects, with their characteristic images, are never seen in this n-type annealed material, implying a concentration of less than 10^{16} cm^{-3}. Higher temperature anneals produce coarsening of the arsenic clusters; results for an additional 800°C, 30 s anneal are shown in Figure 25. The cluster density is found to be about 7×10^{15} cm^{-3} in this case, with a typical diameter of 150 Å. A large cluster is observed near the center of Figure 25a; line cuts through this precipitate at the location indicated by arrows are shown in Figure 25c. The line cuts reveal a characteristic reversal of the topographic contrast with reversed sample-tip bias, as indicated by the arrows. This behavior is a clear indication of local depletion around a charged metal cluster (27, 71). The range of the depletion seen in Figure 25c is about 25 Å. Spectroscopic results from the 1×10^{19} cm^{-3} n-type material, annealed at 600 and 800°C, are shown in Figure 26 (27). For the 600°C anneal, the Fermi level far from the clusters is located near midgap, $E_v + 0.65$ eV, indicating that the depletion spheres of the precipitates overlap. For the 800°C case, the Fermi level is located at $E_v + 1.05$ eV far from the clusters, demonstrating Fermi-level movement toward flat-band conditions. At the clusters, distributions of states extending out from the valence and conduction bands are observed in both spectra. The smaller precipitates (Figure 26a) are certainly not good metals, but the density of midgap states is easily sufficient to provide a charge reservoir for midgap pinning of the Fermi level.

We recently performed STM studies on n- and p-type LTG-GaAs with doping of 1×10^{18} cm^{-3}, annealed at 600°C for 30 min plus 700°C for 30 s. The n-type material revealed a cluster density of 6×10^{16} cm^{-3}, with typical diameter of 80 Å. A close-up view of one precipitate is shown in Figure 27. A depletion sphere around the precipitate, appearing dark in this filled-state conductance image of n-type material, is clearly seen in Figure 27b. The radius of the depletion sphere is about 75 Å [including the white fringe around the dark circle (72)] for this 35-Å radius precipitate. Spectroscopic results, acquired from a point in the LTA-layer far from a cluster are shown in Figure 27c. The characteristic band-gap region of GaAs is seen, but the observed gap is about 2.0 eV, compared with the correct value of 1.4 eV. Thus some tip-induced band bending is clearly occurring in the spectrum. It is well known that tip-induced band bending can occur in STM spectroscopy of low-doped semiconductors (72–74), although the 0.6 eV band bending seen in Figure 27c is significantly larger than that generally observed for 1×10^{18} cm^{-3} doped material. It is likely that the composite nature of this LTG material, containing a collection of depletion spheres, will lead to increased tip-induced band bending. For this 700°C annealed material, carrier activation studies (56, 58) indicate
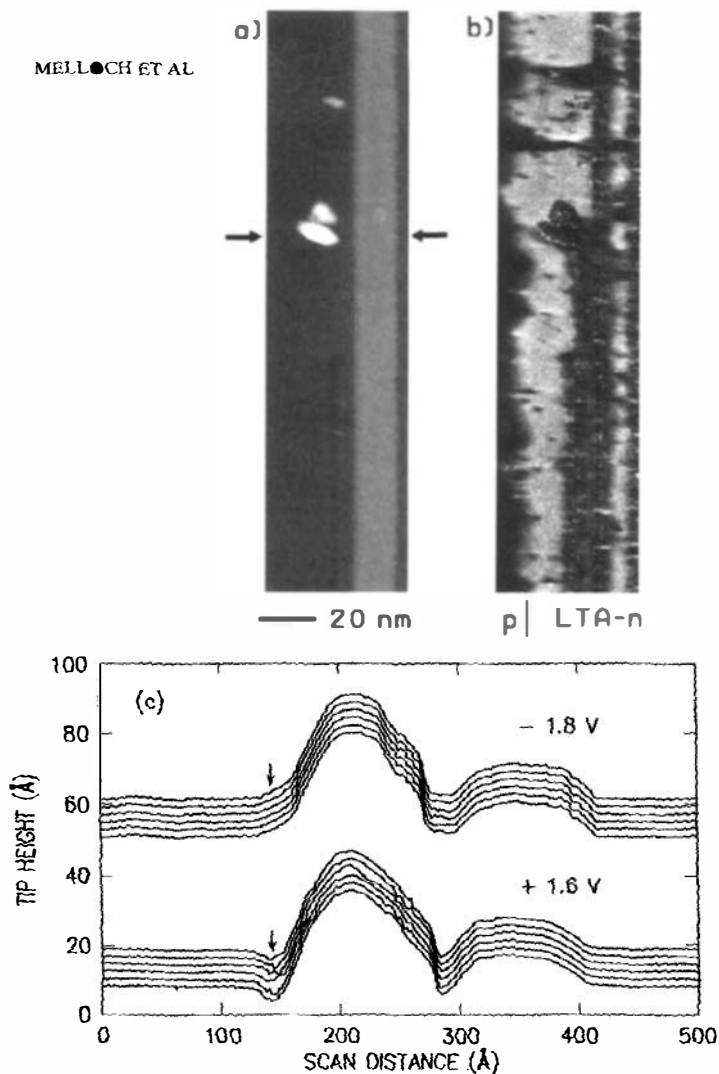
Figure 25   STM image of a cleaved GaAs structure, showing (a) topography and (b) conductance, acquired at a sample voltage of −2.3 V. The gray-scale range in (a) is 33 Å. As indicated in (b), the structure contains an LTA n-type layer, bordered on the left-hand side by a p-type layer grown at higher temperature. The sample was annealed at 800°C. Cross sectional cuts along the line indicated by arrows in (a) are displayed in panel (c), acquired at sample voltages of −1.8 and +1.6 V.
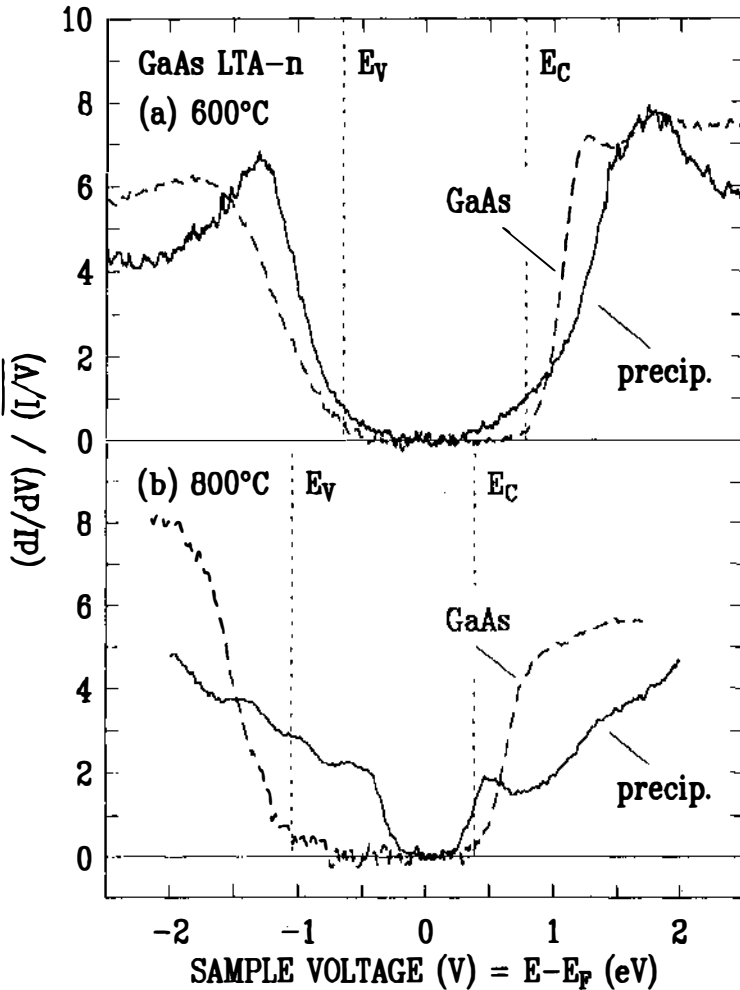
Figure 26 STM spectra acquired from LTA *n*-type layers, annealed at (*a*) 600°C and (*b*) 800°C. Spectra are shown acquired on the arsenic precipitates (*solid line*) and on regions of bare LTA GaAs in between the precipitates (*dashed line*). The valence and conduction band edges are marked by E_V and E_C respectively.

that the depletion spheres are nearly overlapping so that tip-induced band bending will be significant.

According to the buried Schottky barrier model of Figure 14, midgap pinning by the precipitates is expected to lead to depletion regions around each precipitate. The barrier height (or built-in potential) of the depletion regions is related to the depletion radius r_s and cluster radius r_o (Equation
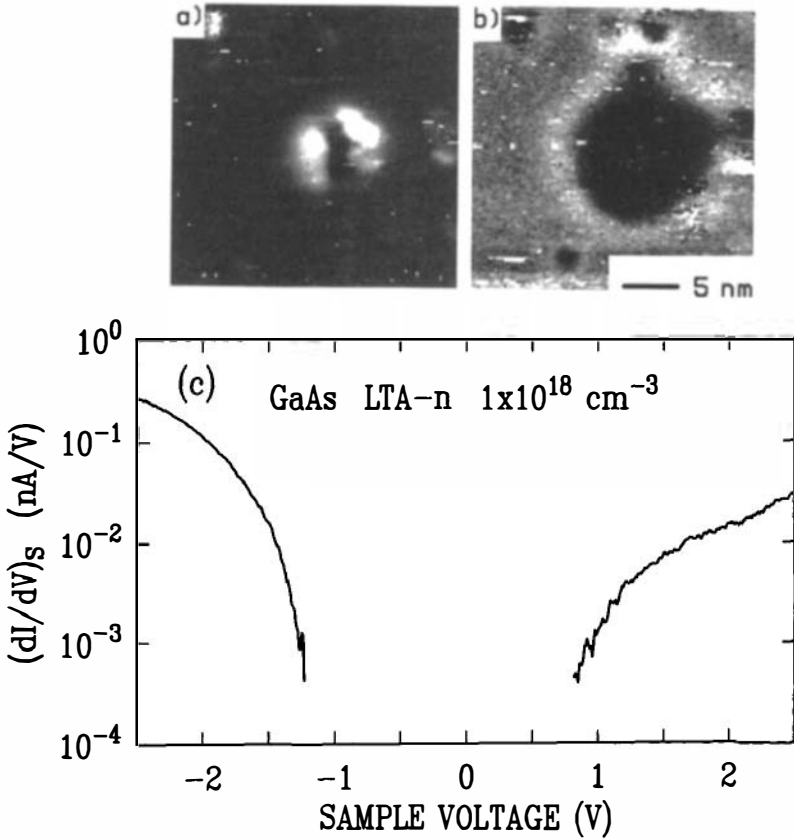
Figure 27   STM image of LTA *n*-type layer, showing (*a*) topography and (*b*) conductance, acquired at a sample voltage of − 2.5 V. The gray-scale range in (*a*) is 2.0 Å. The sample was annealed at 700°C. A tunneling spectrum (conductance at constant tip-sample separation) is shown in (*c*), acquired on a flat region of LTA-GaAs between precipitates.

1). With a barrier height of 0.8 eV for *n*-type material (21), this formula leads to depletion widths r_s-r_o of 90 and 165 Å, respectively for the cases pictured in Figures 25*c* and 27*b*, which are significantly larger than the observed depletion widths of 25 and 40 Å, respectively. One reason for this discrepancy is simply that the nonzero size of the STM probe tip will tend to mask the edges of the precipitates, especially for large clusters such as those seen in Figure 25. In addition, the above-mentioned effects of tip-induced band bending will act to reduce the observed depletion regions. An analogous effect occurs in *pn*-junctions, where for doping levels less than 10^{18} cm^{-3}, observed depletion widths can be significantly smaller than

the actual widths (75) (e.g. in figure 5 of Reference 72 the observed junction width is two times smaller than expected for the $n = 2 \times 10^{17} \, cm^{-3}$ doping).

Figures 28 and 29 display STM results obtained from p-type material with doping concentration of $1 \times 10^{18} \, cm^{-3}$, annealed at 600°C for 30 min, and at 700°C for 30 s. In the topographic image of Figure 28a, clusters appear as the protrusion seen in the center of the image and the depressions seen at the upper and lower edges of the image. The density of clusters in this material is found to be $2 \times 10^{16} \, cm^{-3}$, with typical diameter of 80 Å. Faint white fringes appear around the clusters in the conductance image of Figure 28b, indicative of local band bending in this filled-state image of p-type material. In addition, small point defects, appearing as white points, are seen in the conductance image. Figure 29 shows an expanded view of one point defect. Their appearance is identical to that of the antisite defects seen in the as-grown material, and thus we identify them as being antisite defects. The number of these defects is estimated from the images to be $1.6 \times 10^{18} \, cm^{-3}$, i.e. close to the nominal dopant concentration. Thus within a factor of two, there are just the right number of charged antisites to compensate the bulk acceptors, and the material becomes semi-insulating. Spectroscopic results from this p-type material are shown in the lower part of Figure 29. Tip-induced band bending is very large here, with observed band gaps of about 4 eV, indicating a carrier density many orders of magnitude below the nominal acceptor concentration of $1 \times 10^{18} \, cm^{-3}$.

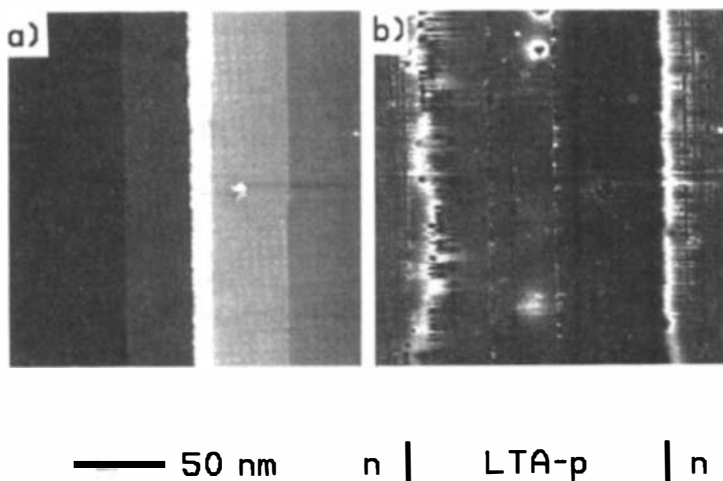50 nm   n | LTA-p | n

Figure 28 STM image of a cleaved GaAs structure, showing (a) topography and (b) conductance, acquired at a sample voltage of -2.2 V. The gray-scale range in (a) is 22 Å. As indicated in (b), the structure contains an LTA p-type layer, surrounded by n-type layers grown at higher temperature. The sample was annealed at 700°C. Several steps occur in the LTA-layer, as seen in (a).
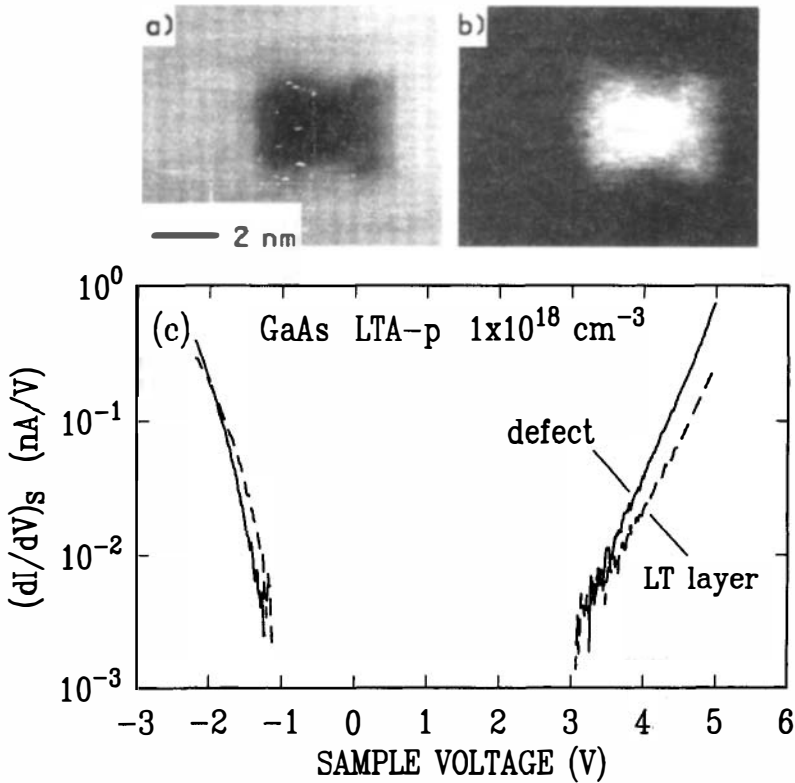
Figure 29 STM image of same sample as in Figure 28, displaying an expanded view of a
point defect (arsenic antisite). Image (*a*) shows topography and (*b*) conductance, acquired at
a sample voltage of -2.2 V. The gray-scale range in (*a*) is 1.1 Å. Tunneling spectra are
shown in (*c*), acquired on the point defect and on a region of flat LTA-GaAs between defects.

Spectra acquired on top of the antisites show a small shift in the band
edge positions, precisely as expected for a charged defect (76). Spectra
acquired on top of the clusters shown in both Figures 27 and 28 display
characteristics similar to those acquired from locations far from the clus-
ters, except that glitches in the spectra are observed on the clusters, indi-
cating charging effects. Apparently, in these cases, the clusters have
insufficient electrical contact to the conductive layers surrounding the
LTG-layer to permit direct observation of midgap states. Nevertheless,
the observed depletion regions around the clusters definitively establish
their effectiveness in Fermi-level pinning.

Summarizing the STM results for annealed LTG-GaAs, one finds that
in *n*-type material, precipitates are observed with no accompanying antisite
defects, whereas in *p*-type material, the two species are found to coexist.

This result is consistent with the formation dynamics of clusters proposed by Melloch et al (15), in which the precipitates form (a) to drive the Fermi level to a midgap position, thereby minimizing the chemical potential, and (b) to minimize the interfacial energy between incorporated arsenic and the GaAs matrix. For p-type material, the midgap pinning position is most effectively obtained by the donor antisite defects, so that in annealed material, a concentration of the antisites equal to the acceptor concentration will remain, and the rest of the arsenic is incorporated in precipitates. In n-type material, the antisite defects, being donors, cannot compensate the shallow donors, so they all form clusters. These precipitates produce midgap pinning, and thus depletion spheres are observed around them. For the case of undoped material, STM observations are not possible, but it is expected that the antisite defect concentration will be low because few if any of the defects are needed for midgap pinning. The relative effect on material properties of residual defects and arsenic clusters depends on their relative concentrations.

Carrier Lifetime

The lifetime of photogenerated carriers in LTG-GaAs is of interest for photoconductive applications of the material (77–81). Harmon et al (82) have used a pump-probe measurement of the differential transmission to determine the lifetime in LTG-GaAs as a function of anneal. A Coherent Mira 900f titanium : sapphire laser was used to produce ~125 fs pulses tuned to a wavelength of 866 nm to measure the GaAs epilayers and tuned to a wavelength of 720 nm to measure the $Al_{0.25}Ga_{0.75}As$ epilayer. These wavelengths were chosen to provide photons of energies about 10 meV above the band gaps to probe the states near the conduction and valence band edges. The pulse from the titanium: sapphire laser, which was running at 73 MHz, was split into a pump and probe beam. The pump beam had an average power of 100 to 200 mW and was focused to a spot size of approximately 50 μm. The probe beam had an average power of 4 to 5 mW and was focused to a slightly smaller spot. The pump beam fills conduction band states and causes a reduction in the absorption. As the electrons recombine, the absorption increases back to its equilibrium value. This transient in the absorption is measured as a function of time, using the probe beam, which is delayed relative to the pump beam by using an Aerotech linear translation stage to vary the optical path length.

The transient responses—plotted as normalized differential transmissions—are shown in Figure 30 for a GaAs epilayer containing 0.9% excess arsenic for different anneal conditions. The carrier lifetime is determined by fitting the transient in Figure 30 with a single exponential. To ensure that the fit is dominated by carrier recombination rather than by
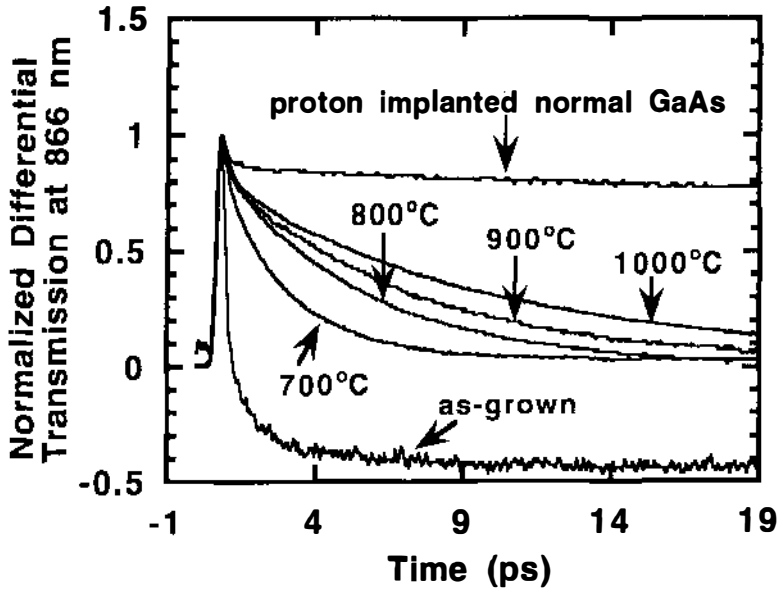
Figure 30 Normalized differential transmission measurements of low-temperature-grown GaAs showing the dependence of the decay of the differential transmission on the arsenic cluster coarsening anneal. The anneals were of duration 30 s at the temperatures indicated. The normal GaAs film is 1-μm MBE material implanted with 1×10^{12} cm^{-2} protons in order to assure recovery to equilibrium between laser pulses.

carrier cooling or system noise, the fit begins 1.5 ps after the peak and extends to the point where the transient reaches 10% of the final value. The results of carrier lifetime vs precipitate spacing are shown in Figure 31 for a GaAs epilayer containing 0.9% excess arsenic, a GaAs epilayer containing 0.7% excess arsenic, a GaAs epilayer containing 0.3% excess arsenic, and an $Al_{0.25}Ga_{0.75}As$ epilayer containing 0.2% excess arsenic. These results indicate an increase in carrier lifetime with an increase in precipitate spacing.

To interpret the data in Figure 31, a single recombination center is assumed. The carrier lifetime can be described by

$$\tau = \frac{1}{\sigma N v_t} \qquad 5.$$

where σ is the capture cross section of the trap, N is the number of empty traps, and v_t is the electron thermal velocity. If we suppose the trap is the arsenic cluster, then we would expect the capture cross section to be proportional to the area of the precipitate. This model does not accurately describe the observed trends because the GaAs epilayer with 0.3% excess
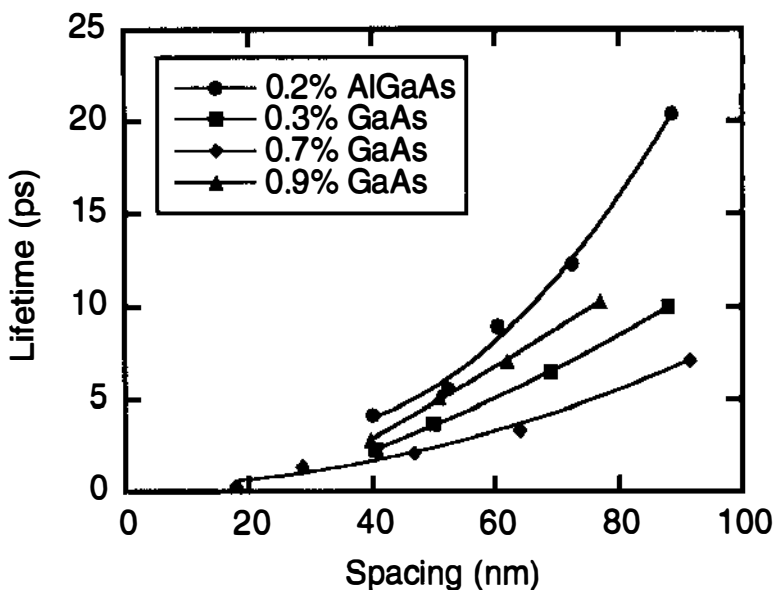
Figure 31 Carrier lifetime vs cluster spacing, fit by a square dependence on cluster spacing
for four epilayers. Three of the epilayers are GaAs, one containing 0.3% excess arsenic, one
containing 0.7% excess arsenic, and one with 0.9% excess arsenic. The fourth epilayer is
AlGaAs containing 0.2% excess arsenic.

arsenic has a shorter carrier lifetime than the GaAs epilayer with 0.9%
excess arsenic when the cluster spacings are the same. For the same arsenic
cluster spacing, one would expect the GaAs epilayer with 0.9% excess
arsenic to have the shorter carrier lifetime because the arsenic clusters are
larger—hence the capture cross section is larger. In addition to the arsenic
clusters, it is possible that other point defects affect the carrier lifetimes.
However, Equation 5 describes a system of traps capable of absorbing
only one electron at a time. For a system containing traps that can be
multiply ionized, there would be terms of the form of Equation 5 for
each ionization level. The arsenic precipitates, indeed, can accept many
electrons and are perhaps better thought of as sinks for electrons rather
than discrete, single-electron traps. In this view, electron removal from the
GaAs matrix is limited by diffusive transport to the precipitates rather
than random thermal impacting on the precipitates. This model predicts
a square dependence of measured lifetime to precipitate spacing, which is
in better agreement with the results observed. A square dependence of
the carrier lifetime with the spacing between clusters is observed in the
experimental data illustrated in Figure 31—the variation of lifetime in the
three films for a given arsenic cluster spacing is the result of differences in

mobilities. For the same arsenic cluster spacing, we would expect the GaAs region between arsenic clusters in the epilayer with 0.9% excess arsenic to have a lower mobility (more initial strain and point defects) than the GaAs region between arsenic clusters in the epilayer with 0.3% excess arsenic.

DEVICE APPLICATIONS

Buffer Layers

The first device application of LTG-GaAs was as a buffer layer under MESFETs (4, 5). Smith et al (5) found that such a buffer layer grown at 200°C, which was subsequently annealed when the top epilayer was grown for the MESFET, resulted in a complete elimination of side-gating. Subsequently, Lin et al (83) demonstrated the use of LTG-GaAs to eliminate side-gating in HEMTs; however, they also discovered that non-optimized LTG-buffer structures resulted in outdiffusion of defects from the LTG buffer to the active regions, resulting in degradation of the high-frequency performance. Lin et al (83) used a multi-substrate temperature procedure during MBE of the buffer regions to minimize this effect. Solomon et al (84) also have used a LTG-GaAs layer to reduce back-gating in GaAs semiconductor-insulator-semiconductor FETs (SISFETs).

Another application of LTG-GaAs for MESFETs was the placement of the LTG-GaAs region on top of the MESFET channel to improve the breakdown voltage (46). Lin et al (46) discovered that they needed a 20-nm AlAs layer between the LTG-GaAs and the n-GaAs channel to prevent arsenic and Ga-vacancy diffusion from the LTG-GaAs layer into the n-GaAs channel, which would compensate the channel. Substantial enhancement of the breakdown voltage was achieved without degradation of the drive capability of the MESFET.

The semi-insulating properties have also been used for isolation in optical devices. Subramanian et al (85) have demonstrated the utility of GaAs : As for isolation between tandem solar cells. There have also been many demonstrations of the applications of GaAs : As as a current-blocking layer in diode lasers (86–88).

Photoconductors

Because these composites are semi-insulating, exhibit reasonable mobilities, and in some cases subpicosecond lifetimes (77–79), they are attractive materials for applications where one needs a high-speed photoconductor. GaAs : As has been used as the photoconducting switch to launch freely propagating electromagnetic pulses (79–81). The freely propagating electromagnetic pulses have applications for radar systems. Rahman et al (81) have used LTG-GaAs to photoconductively switch coplanar-strip

antennas to generate picosecond bursts of freely propagating electro-magnetic energy, which was used for measuring target resonances.

Because the arsenic precipitates form embedded Schottky barriers, it is possible to detect light with photon energies below the band gap of the semiconductor matrix, relying on internal photoemission from the arsenic precipitates. Using this concept, GaAs-based *p-i-n* photodiodes have been demonstrated with reasonable room-temperature responsivities out to 1.7 μm by incorporating a composite as the *i*-layer (89, 90). The below-band-gap responsivity is the result of internal photoemission from the arsenic precipitates in the *i*-layer. This below-band-gap response is illustrated in Figure 32 for a GaAs (25) and an AlGaAs (91) *p-i-n* diode. The *i*-layers in these two diodes were grown at 250°C to incorporate excess arsenic. Upon raising the substrate temperature to 600°C to grow the top *p*-layers, the excess arsenic precipitates, forming the composite *i*-layer. Linear extra-polation of the curves in Figure 32 results in internal barrier heights of 0.7 eV for GaAs:As and 0.94 eV for $Al_{0.25}Ga_{0.75}As$:As.

Below band-gap, metal-semiconductor-metal photodetectors (MSM-PDs) on GaAs:As have also been investigated (92). The MSM-PD was buried within a ground-signal-ground coplanar stripline, with the Ti/Pt/Au
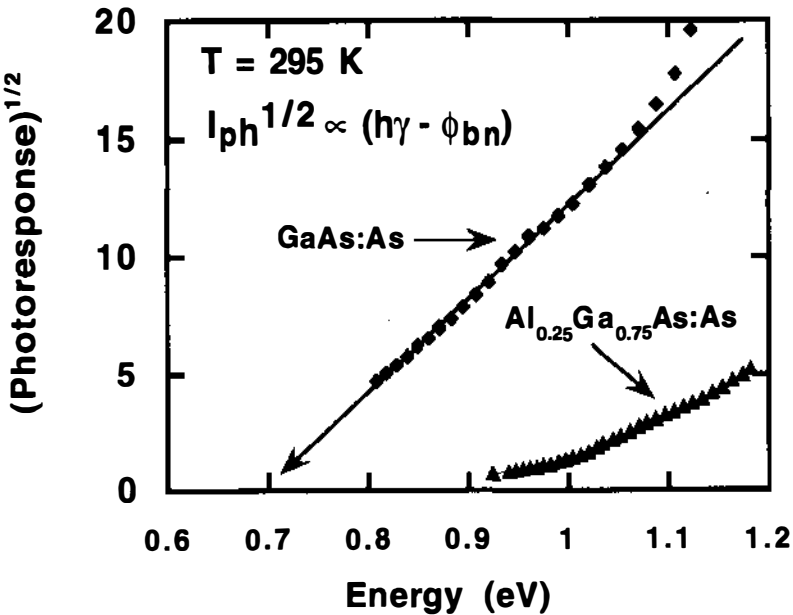
Figure 32   Photoresponse vs photon energy for two PiN diodes. One *p-i-n* diode has an *i*-layer of GaAs containing arsenic clusters, and the other has an *i*-layer of $Al_{0.25}Ga_{0.75}As$ containing arsenic clusters. The *p*- and *n*-regions are normal highly stoichiometric material.

MSM-PD fingers and striplines defined in one mask step. The detector area was $75 \times 75 \ \mu m^2$, with finger spacing of 3 μm. The optical excitation used was 1.3-μm pulses of width 700 to 900 fs. The generated electrical pulse was coupled into a 40 GHz Tektronix sampling head. The total system rise time was 13 ps. The measured pulse response was at the system limit, with 10 to 90% rise and fall times of about 14 ps, independent of bias from 2–35 V. Integration of the pulse produced an estimated responsivity of 0.25 mA/W. By deconvolving the response of the probe and the scope from the temporal measurement, a detector bandwidth well beyond 50 GHz was estimated.

Although light below the band gap of the semiconductor matrix can be detected by internal photoemission from the arsenic clusters, the responsivity is low because of the low absorption of the incident photons. Recently, devices have been exhibited that use internal gain to increase the responsivity. One was a HEMT version, where the HEMT channel was grown at low temperatures and thus contained arsenic clusters (93). The other was a photoconductor with an n-GaAs:As channel and ohmic contacts separated by 1 μm, as illustrated in Figure 33 (94). The device in Figure 33 was annealed so that the precipitates coarsen to a point where the channel is just depleted. This device exhibits gain for both above- and below-band-gap illumination. The gain is a consequence of an increase in carrier lifetime due to the band bending present because of the n-type doping. For above-band-gap illumination, the holes and electron are separated by the band bending, with the holes going to the precipitates and the electrons staying in the conducting channels between the precipitates. Similarly for below-band-gap illumination, the electrons emitted from the precipitates are contained in the regions between the precipitates due to
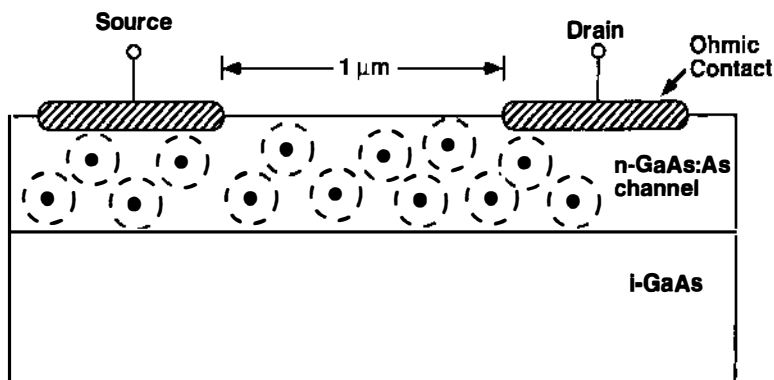

Figure 33 Cross section of metal-semiconductor-metal photoconductor showing depletion regions surrounding the arsenic precipitates in the channel.

the band bending. This effectively increases the lifetime of photogenerated electrons because the electrons are prevented from recombining at the precipitates by internal electric fields, thus resulting in a photoconductive gain effect. The greater the density of photogenerated electrons, the smaller the effective increase in electron lifetimes because the higher hole concentration on the precipitates reduces the band bending. Therefore, one is trading bandwidth for gain (responsivity) with these devices. Shown in Figure 34 is the photocurrent as a function of bias, with illumination power as a parameter, for 850-nm illumination (Figure 34a) and for 950-nm illumination (Figure 34b). The saturation in the photocurrent is caused by velocity saturation. The responsivity as a function of wavelength is shown in Figure 35 with optical power as a parameter. The responsivity varies considerably with input power, which indicates that the gain of the device varies with input power, consistent with the argument above for the decrease in carrier lifetime with increase in illumination intensity.

Nonlinear Optics

LTG technology has opened the door to a new class of nonlinear-optical applications, called photorefractive nanostructures, that require semi-insulating quantum well structures. Photorefractive quantum wells (95–98) are photo-active semiconductor thin films that can be used to record time-varying holograms. Such dynamic holographic media will form the core of future imaging applications that range from parts inspection on assembly lines, to error removal in high-data-rate fiber telecommunications, to information processing in optical computers.

LTG materials have moved into several key functional roles in the designs of photorefractive nanostructures. The value of the LTG material for holography lies in their high defect densities and their ultrafast carrier lifetimes. One of the most important issues during hologram recording is the density of optical information storage. This data density is limited primarily by carrier diffusion, with the minimum data spacing given by $L = 2\pi L_D$, where L_D is the diffusion length. The ultrafast lifetimes in LTG layers (82) produce ultrashort diffusion lengths down to 0.1 μm, yielding two-dimensional data densities of 3×10^8 bits/cm^2. These high data densities were demonstrated experimentally in LTG GaAs thin films (99).

In photorefractive experiments, the LTG layer performed as the short-transport-length material as well as an electro-optic layer. Photorefractive effects need electro-optic effects such as electric field–induced changes in the exciton absorption. But the excitonic transitions in LTG materials with large excess arsenic concentrations are severely broadened, making them appear less useful for electro-optic applications (100). However, it was discovered that the excitonic transitions in strongly annealed LTG-
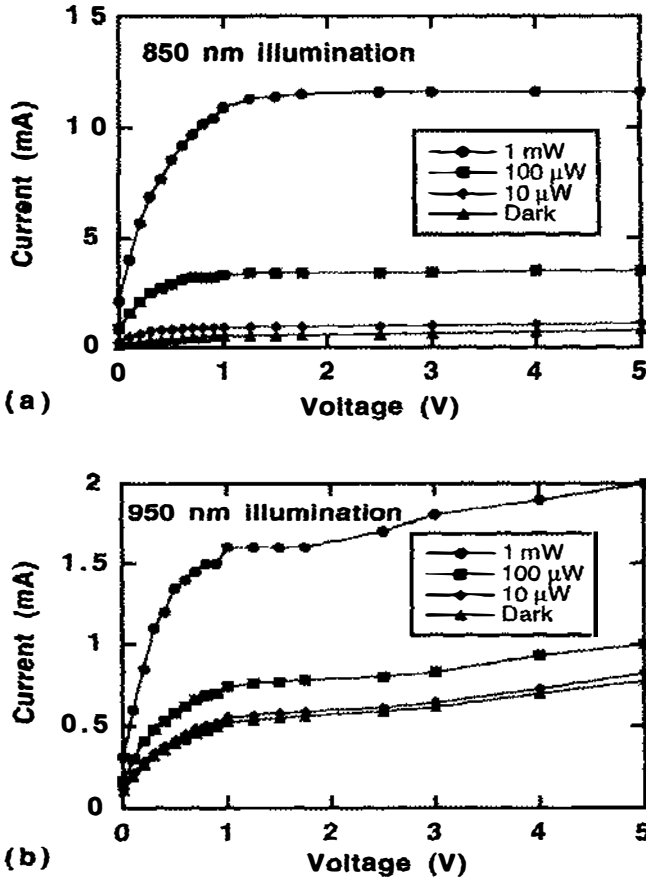
Figure 34 Current-voltage characteristics of the Figure 23 photodetector with 1-μm finger spacing under (*a*) 850- and (*b*) 950-nm illumination.

AlGaAs were particularly sensitive to applied electric fields, producing large electro-optic effects at low field strengths that exceeded the quantum-confined Stark effect at comparable fields, as shown in Figure 36 (101, 102). The excitons in the LTG material responded to applied electric fields as if a much larger field had been applied. It has been suggested (92, 103) that the arsenic precipitates become highly charged during current transport, leading to internal microfields that can significantly exceed
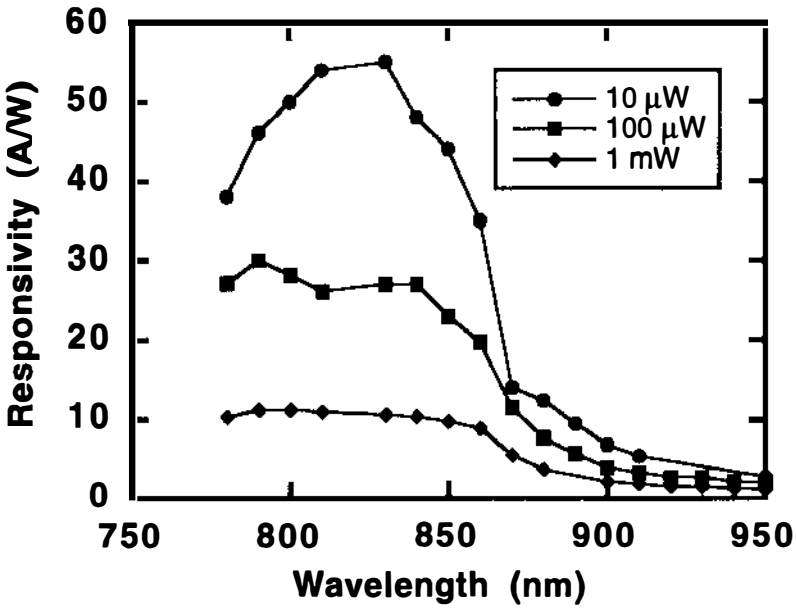
Figure 35 Responsivity vs wavelength of the Figure 23 photodetector with optical power
as a parameter.
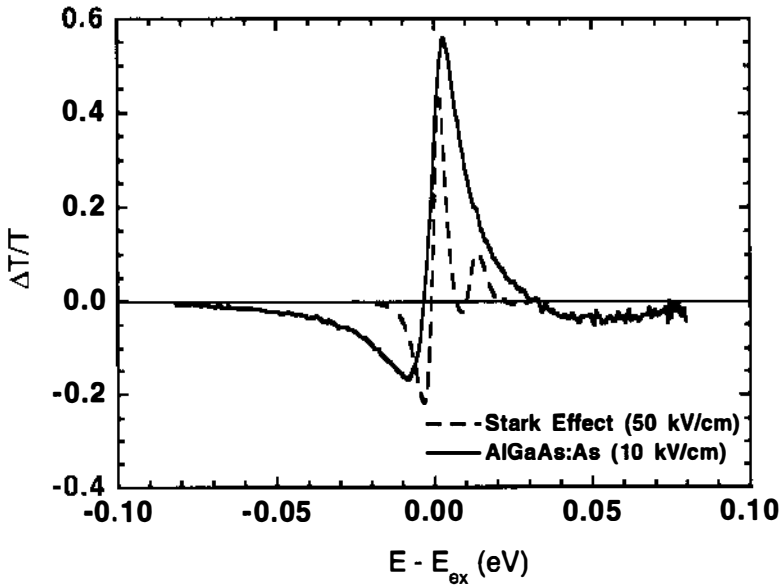
Figure 36 Comparison of the quantum-confined Stark effect in a high-quality, highly
stoichiometric multiple-quantum well structure and in an AlGaAs epilayer containing arsenic
clusters.

macroscopic fields. This electro-optic mechanism represents a fundamental departure from traditional electro-optic mechanisms that rely entirely on macroscopic fields. Furthermore, the broadened excitons in the LTG materials lead to broad-band electro-optic modulation, which can be important for femtosecond pulse applications (104), or for other broad-band applications such as wavelength-division multiplexing.

More complicated photorefractive quantum wells structures have recently incorporated LTG layers as ultrafast trapping layers to store space charge (105, 106). The LTG layers in these structures were not used for electro-optic properties. Traditional high-temperature grown quantum wells provided quantum-confined excitons with large quantum-confined Stark effects. These quantum wells required proton implantation to make them semi-insulating, which complicates the device processing. Recent studies of LTG multiple quantum wells grown at moderate temperatures (107) have exhibited extremely sharp excitonic transitions, with large quantum-confined Stark shifts that produce absorption changes up to $\Delta\alpha = 9000$ cm^{-1}. This ability to grow high-quality semi-insulating multiple quantum well structures with sharp excitonic features had been an elusive goal. The discovery of sharp spectra in LTG quantum wells makes this material an important new option for many electro-optic applications.

Non-Alloyed Ohmic Contacts

The dominant contact technology for GaAs-based devices includes an alloying step, which makes these contacts unsuitable as optical mirrors. Yamamoto et al (108) have shown that ex situ non-alloyed contacts can be formed on LTG-GaAs with a specific resistivity of 1.5×10^{-3} Ω-cm^2. Patkar et al (109) have further developed non-alloyed contact technology based on LTG epilayers for both p- and n-GaAs, demonstrating a three-order-of-magnitude reduction in specific contact resistivity to n-GaAs as compared with results from Yamamoto et al (108). The fact that these contacts are non-alloyed opens the possibility of their use as optical mirrors in applications such as solar cells, light-emitting diodes (LEDs), and vertical-cavity surface-emitting lasers (VCSELs).

Low-temperature growth has been used in the past to improve the Be-doping efficiency in GaAs (110) and InGaAs devices (111, 112). When doping GaAs p-type with Be during MBE, hole concentrations greater than 10^{20} cm^{-3} can be achieved with substrate temperatures in the range of 300 to 400°C due to a slight arsenic excess in the epilayer. If this LTG p-GaAs is annealed subsequently, with an arsenic over-pressure, the excess arsenic in the bulk ensures that any interstitial Be atoms are driven onto acceptor sites, whereas the excess arsenic should go onto regular arsenic

sites in the lattice. A non-alloyed ohmic contact is readily formed when metal is deposited on such a heavily doped layer due to holes tunneling through the narrow depletion region. Patkar et al (109) have demonstrated tunneling contact resistances of $< 10^{-6}$ Ω-cm^2 to such LTG-p-GaAs epilayers.

Achieving high n-type doping concentrations is more difficult than achieving high p-type concentrations in bulk GaAs. Silicon is the typical n-type dopant used in MBE of GaAs. In a depletion region, Si atoms on Ga sites (the donor site) can approach 10^{20} cm^{-3}, which is the case for the near-surface during MBE (113). However, the electron concentration in the bulk of the GaAs—below the surface depletion region—reverts to only 5×10^{18} cm^{-3} because of a large fraction of the Si atoms switching to arsenic sites. Upon removal from the MBE system and exposure of the n-GaAs surface to the atmosphere, the near-surface, heavily n-doped region oxidizes—unlike a heavily p-doped GaAs surface that is resistant to oxidation. A metal deposited on this oxidized, n-GaAs surface will not form an ohmic contact. Patkar et al (109) have found that a thin, 1- to 2-nm undoped GaAs layer that contains about 1% excess arsenic can be used to protect the $> 10^{20}$ cm^{-3} donor density GaAs region. After air exposure of these surfaces, deposition of Ti, Ag, or Au results in ohmic contacts with a specific contact resistance of $< 10^{-6}$ Ω-cm^2.

SUMMARY

In summary, GaAs, AlGaAs, and InGaAs epilayers containing excess arsenic are interesting new materials. The nature of the material can be dramatically changed by annealing from a material with large concentrations of point defects to a two-phase system of metallic arsenic clusters in an arsenide semiconductor matrix. The two-phase form shows promise for many electronic and optoelectronic applications.

Literature Cited

1. Cho AY, Arthur JR. 1975. *Prog. Solid State Chem.* 10: 157–91
2. Cho AY. 1970. *J. Appl. Phys.* 41: 2780–86
3. Foxon CT, Joyce BA. 1977. *Surf. Sci.* 64: 293–305
4. Murotani T, Shimanoe T, Mitsui S. 1978. *J. Cryst. Growth* 45: 302–8
5. Smith FW, Calawa AR, Chen C-L, Mantra MJ, Mahoney LJ. 1988. *IEEE Electron Device Lett.* 9: 77–80
6. Melloch MR, Miller DC, Das B. 1989. *Appl. Phys. Lett.* 54: 943–45
7. Kaminska M, Weber ER, Liliental-Weber Z, Leon R, Rek ZU. 1989. *J. Vac. Sci. Technol. B* 7: 710–13
8. Melloch MR, Otsuka N, Woodall JM, Warren AC, Freeouf JL. 1990. *Appl. Phys. Lett.* 57: 1531–33
9. Kaminska M, Liliental-Weber Z, Weber ER, George T, Kortright JB, et al. 1989. *Appl. Phys. Lett.* 54: 1881–83
10. Melloch MR, Mahalingam K, Otsuka N, Woodall JM, Warren AC. 1991. *J. Cryst. Growth* 111: 39–42
11. Liliental-Weber Z, Cooper G, Mariella R Jr, Kocot C. 1991. *J. Vac. Sci. Technol. B* 9: 2323–27
12. Mahalingam K, Otsuka N, Melloch MR, Woodall JM, Warren AC. 1991. *J. Vac. Sci. Technol. B* 9: 2328–32
13. Mahalingam K, Otsuka N, Melloch MR, Woodall JM. 1992. *Appl. Phys. Lett.* 60: 3253–55
14. Melloch MR, Otsuka N, Mahalingam K, Chang CL, Kirchner PD, et al. 1992. *Appl. Phys. Lett.* 61: 177–79
15. Melloch MR, Otsuka N, Mahalingam K, Chang CL, Woodall JM, et al. 1992. *J. Appl. Phys.* 72: 3509–13
16. Ibbetson JP, Speck JS, Gossard AC, Mishra UK. 1993. *Appl. Phys. Lett.* 62: 169–71
17. Ibbetson JP, Speck JS, Gossard AC, Mishra UK. 1993. *Appl. Phys. Lett.* 62: 2209–11
18. Melloch MR, Woodall JM, Otsuka N, Mahalingam K, Chang CL, et al. 1993. *Mater. Sci. Eng. B* 22: 31–36
19. Cheng TM, Chin A, Chang CY, Huang MF, Hsieh KY, Huang JH. 1994. *Appl. Phys. Lett.* 64: 1546–48
20. Baranowski JM, Liliental-Weber Z, Yau W-F, Weber ER. 1991. *Phys. Rev. Lett.* 66: 3079–3082
21. Warren AC, Woodall JM, Freeouf JL, Grischkowsky D, McInturff DT, et al. 1990. *Appl. Phys. Lett.* 57: 1331–33
22. Verma AK, Tu J, Smith JS, Fujioka H, Weber E. 1993. *J. Electron. Mater.* 22: 1417–20
23. Ibbetson JP, Speck JS, Nguyen NX, Gossard AC, Mishra UK. 1993. *J. Electron. Mater.* 22: 1421–24
24. Fang Z-Q, Look DC. 1993. *J. Electron. Mater.* 22: 1429–32
25. McInturff DT, Woodall JM, Warren AC, Braslau N, Pettit GD, et al. 1992. *Appl. Phys. Lett.* 60: 448–50
26. Jager ND, Verma AK, Dreszer P, Newman N, Liliental-Weber Z, et al. 1993. *J. Electron. Mater.* 22: 1499–1502
27. Feenstra RM, Vaterlaus A, Woodall JM, Pettit GD. 1993. *Appl. Phys. Lett.* 63: 2528–30
28. Cho AY. 1969. *Surf. Sci.* 17: 494–503
29. Eaglesham DJ, Pfeiffer LN, West KW, Dykaar DR. 1991. *Appl. Phys. Lett.* 58: 65–67
30. Liliental-Weber Z, Swider W, Yu KM, Kortright J, Smith FW, Calawa AR. 1991. *Appl. Phys. Lett.* 58: 2153–55
31. Ibbetson JP, Mirin RP, Mishra UK, Gossard AC. 1994. *J. Vac. Sci. Technol. B* 12: 1050–52
32. Wie CR, Xie K, Look DC, Evans KR, Stutz CE. 1991. *Mater. Res. Soc. Symp. Proc.* 198: 178
33. Matyi RJ, Melloch MR, Woodall JM. 1992. *Appl. Phys. Lett.* 60: 2642–44
34. Liliental-Weber Z, Claverie A, Washburn J, Smith FW, Calawa AR. 1991. *Appl. Phys. A* 53: 141–46
35. Matyi RJ, Melloch MR, Woodall JM. 1993. *J. Cryst. Growth* 129: 719–27
36. Voorhees PW. 1985. *J. Stat. Phys.* 38: 231–52
37. Köhler K, Ganser P, Maier M. 1993. *J. Cryst. Growth* 127: 720–23
38. Manasreh MO, Stutz CE, Solomon JG, Mier MG, Kaspi R, Evans KR. 1993. In *Semi-Insulating III-V Materials*, ed. GJ Miner, W Ford, ER Weber, Ixtapa, Mexico, 1992. Bristol: Inst. Phys.

39. McQuaid SA, Newman RC, Missous M, O'Hagan S. 1992. *Appl. Phys. Lett.* 61: 3008–10

40. O'Hagan S, Missous M. 1994. *J. Appl. Phys.* 75: 7835–41

41. Cheng TM, Chang CY, Chang TC, Huang JH, Huang MF. 1994. *Appl. Phys. Lett.* 64: 3626–28

42. Mahalingam K, Otsuka N, Melloch MR, Woodall JM, Warren AC. 1992. *J. Vac. Sci. Technol. B* 10: 812–14

43. Cheng TM, Chang CY, Chin A, Huang MF, Huang JH. 1994. *Appl. Phys. Lett.* 64: 2517–19

44. Melloch MR, Chang CL, Otsuka N, Mahalingam K, Woodall JM, Kirchner PD. 1993. *J. Cryst. Growth* 127: 499–502

45. Horikoshi Y, Kawashima M, Yamaguchi H. 1986. *Jpn. J. Appl. Phys.* 25: L868–70

46. Yin L-W, Hwang Y, Lee JH, Kolbas RM, Trew RJ, Mishra UK. 1990. *IEEE Electron Device Lett.* 11: 561–63

47. Claverie A, Namavar F, Liliental-Weber Z. 1993. *Appl. Phys. Lett.* 62: 1271–73

48. Chang JCP, Otsuka N, Harmon ES, Melloch MR, Woodall JM. 1994. *Appl. Phys. Lett.* 65: 2801–3

49. Nolte DD. 1994. *J. Appl. Phys.* 76: 3740–45

50. Manasreh MO, Look DC, Evans KR, Stutz CE. 1990. *Phys. Rev. B* 41: 10272–75

51. Look DC, Walters DC, Mier M, Stutz CE, Brierley SK. 1992. *Appl. Phys. Lett.* 60: 2900–2

52. Look DC, Walters DC, Manasreh MO, Sizelove JR, Stutz CE, Evans KR. 1990. *Phys. Rev. B* 42: 3578–81

53. Campbell AC, Crook GE, Rogers TJ, Streetman BG. 1990. *J. Vac. Sci. Technol. B* 8: 305–7

54. Look DC, Robinson GD, Sizelove JR, Stutz CE. 1993. *J. Electron. Mater.* 22: 1425–28

55. Look DC. 1991. *J. Appl. Phys.* 70: 3148–51

56. Warren AC, Woodall JM, Kirchner PD, Yin X, Pollak FH, et al. 1992. *Phys. Rev. B* 46: 4617–20

57. Rossi DV, Fossum ER, Pettit GD, Kirchner PD, Woodall JM. 1987. *J. Vac. Sci. Technol. B* 5: 982–84

58. Atique N, Harmon ES, Chang JCP, Woodall JM, Melloch MR. 1995. *J. Appl. Phys.* 77: 1471–76

59. Bliss DE, Walukiewicz W, Ager JW, Haller EE, Chan KT, Tanigawa S. 1992. *J. Appl. Phys.* 71: 1699–1707

60. Pollak FH, Shen H. 1993. *Mater. Sci. Eng. Rep.* 10: 275–374

61. Warren AC, Woodall JM, Kirchner PD, Yin X, Guo X, et al. 1992. *J. Vac. Sci. Technol. B* 10: 1904–7

62. Warren AC, Woodall JM, Borroughes JH, Kirchner PD, Heinrich HK, et al. 1992. *Mater. Res. Soc. Symp. Proc.* 241: 15–25

63. Shen H, Rong FC, Lux R, Pamulapati J, Dutta M, et al. 1992. *Appl. Phys. Lett.* 61: 1585–87

64. Shen H, Rong FC, Lux R, Pamulapati J, Dutta M, et al. 1992. *Proc. Soc. Photo-Opt. Instrum. Eng.* 1678: 211

65. Look DC, Hoelscher JE, Grant JT, Stutz CE, Evans KR, Numan M. 1992. *Mater. Res. Soc. Symp. Proc.* 241: 87–92

66. Woodall JM, Kirchner PD, Freeouf JL, McInturff DT, Melloch MR, Pollak FH. 1993. *Philos. Trans. R. Soc. London Ser. A* 344: 521–32

67. Yin X, Chen H-M, Pollak FH, Cao Y, Montano PA, et al. 1991. *J. Vac. Sci. Technol. B* 9: 2114–17

68. Feenstra RM, Woodall JM, Pettit GD. 1994. *Mater. Sci. Forum* 143–147: 1311–18

69. Feenstra RM, Woodall JM, Pettit GD. 1993. *Phys. Rev. Lett.* 71: 1176–79

70. Feenstra RM. 1994. *Semicond. Sci. Technol.* 9: 2157–68

71. Feenstra RM, Martensson P. 1988. *Proc. 19th Int. Conf. Phys. Semiconductors*, ed. W Zawadzki, pp. 629–36. Warsaw: Polish Inst. Phys.

72. Feenstra RM, Vaterlaus A, Yu ET, Kirchner PD, Lin CL, et al. 1993. *Semiconductor Interfaces at the Sub-Nanometer Scale*, ed. HWM Salemink, MD Pashley, pp. 127–37. Netherlands: Kluwer

73. Feenstra RM, Stroscio JA. 1987. *J. Vac. Sci. Technol. B* 5: 923–29

74. Feenstra RM. 1994. *Phys. Rev. B* 50: 4561–70

75. Chapman R, Kellam M, Goodwin-Johansson S, Russ J, McGuire GE. 1992. *J. Vac. Sci. Technol. B* 10: 502–7

76. Stroscio JA, Feenstra RM. 1988. *J. Vac. Sci. Technol. B* 6: 1472–78

77. Smith FW, Lee HW, Diadiuk V, Hollis MA, Calawa AR, et al. 1989. *Appl. Phys. Lett.* 54: 890–92

78. Gupta S, Battacharya PK, Pamaulapati J, Mourou G. 1990. *Appl. Phys. Lett.* 57: 1543–45

79. Warren AC, Katzenellenbogen N, Grischkowsky D, Woodall JM, Melloch MR, Otsuka N. 1991. *Appl. Phys. Lett.* 58: 1512–14

80. Carin L, Kralij DR, Melloch MR, Woodall JM. 1993. *IEEE Microwave Guided Wave Lett.* 3: 339–41

81. Rahman A, Kralj D, Carin L, Melloch MR, Woodall JM. 1994. *Appl. Phys. Lett.* 64: 2178–80
82. Harmon ES, Melloch MR, Woodall JM, Nolte DD, Otsuka N, Chang CL. 1993. *Appl. Phys. Lett.* 63: 2248–50
83. Lin BJF, Kocot CP, Mars DE, Jaeger R. 1990. *IEEE Trans. Electron Devices* 37: 46–50
84. Solomon PM, Wright SL, Canora FJ. 1991. *IEEE Electron Device Lett.* 12: 117–19
85. Subramanian G, Dodabalapur A, Campbell JC, Streetman BG. 1991. *Appl. Phys. Lett.* 58: 2514–16
86. Sin YK, Horikawa H, Matsuyama I, Kamijoh T. 1992. *Electron. Lett.* 28: 803–4
87. Rogers TJ, Lei C, Streetman BG, Deppe DG. 1993. *J. Vac. Sci. Technol. B* 11: 926–28
88. Takamori T, Sin YK, Watanabe K, Kamijoh T. 1992. *Appl. Phys. Lett.* 61: 2266–68
89. Warren AC, Burroughes JH, Woodall JM, McInturffDT, Hodgson RT, Melloch MR. 1991. *IEEE Electron Device Lett.* 12: 527–29
90. Srinivasan A, Sadra K, Campbell JC, Streetman BG. 1993. *J. Electron. Mater.* 22: 1457–59
91. McInturff DT, Woodall JM, Warren AC, Braslou N, Pettit GD, et al. 1993. *Appl. Phys. Lett.* 62: 2367–68
92. Melloch MR, Otsuka N, Harmon ES, Nolte DD, Woodall JM, McInturff DT. 1993. *J. Jpn. Appl. Phys.* 32: 771–74
93. Subramaniam S, Schulte D, Ungier L, Zhao P, Plant TK, Arthur JR. 1995. *IEEE Electron Device Lett.* 16: 20–22
94. Harmon ES, McInturff DT, Melloch MR, Woodall JM. 1995. *J. Vac. Sci. Technol. B* 13: In press
95. Nolte DD, Melloch MR. 1995. In *Photorefractive Effects Materials*, ed. DD Nolte, 7: 373–451. Dordrecht: Kluwer
96. Nolte DD, Olson DH, Doran GE, Knox WH, Glass AM. 1990. *J. Opt. Soc. Am. B* 7: 2217–25
97. Wang QN, Brubaker RM, Nolte DD, Melloch MR. 1994. *J. Opt. Soc. Am. B* 9: 1626–41
98. Nolte DD, Melloch MR. 1994. *MRS Bull.* 19: 44–49
99. Nolte DD, Melloch MR, Ralph SE, Woodall JM. 1992. *Appl. Phys. Lett.* 61: 3098–3100
100. Knox WH, Doran GE, Asom M, Livescu G, Leibenguth R, Chu SNG. 1991. *Appl. Phys. Lett.* 59: 1491–93
101. Nolte DD, Melloch MR, Woodall JM, Ralph SJ. 1993. *Appl. Phys. Lett.* 62: 1356–58
102. Melloch MR, Nolte DD, Otsuka N, Chang CL, Woodall JM. 1993. *J. Vac. Sci. Technol. B* 10: 795–97
103. Nolte DD, Lahiri I, McKenna J, Steldt FR, Chang JCP, et al. 1994. In *Proc. 22nd Int. Conf. Phys. Semicond. Vancouver, BC, Canada*
104. Weiner AM, Leaird DE, Reitze DH, Paek EG. 1992. *IEEE J. Quantum Electron.* 28: 2251–61
105. Partovi A, Glass AM, Olson DH, Zydzik GJ, O'Bryan HM, et al. 1993. *Appl. Phys. Lett.* 62: 464–66
106. Kyono CS, Ikossi-Anastasiou K, Rabinovich WS, Bowman SR, Katzer DS. 1994. *Appl. Phys. Lett.* 64: 2244–46
107. Lahiri I, Nolte DD, Harmon ES, Melloch MR, Woodall JM. 1995. *Appl. Phys. Lett.* Submitted
108. Yamamoto H, Fand Z-Q, Look DC. 1990. *Appl. Phys. Lett.* 57: 1537–39
109. Patkar MP, Chin TP, Woodall JM, Lundstrom MS, Melloch MR. 1995. *Appl. Phys. Lett.* 66: 1412–14
110. Lievin JL, Dubon-Chevallier C, Alexandre F, Leroux G, Dangla J, Ankri D. 1986. *IEEE Electron Device Lett.* 7: 129–31
111. Hamm RA, Panis MB, Nottenburg RN, Chen YK, Humphrey DA. 1989. *Appl. Phys. Lett.* 54: 2586–88
112. Metzger RA, Hafiji M, Stanchina WE, Liu T, Wilson RG, McCray LG. 1993. *Appl. Phys. Lett.* 63: 1360–62
113. Kirchner PD, Jackson TN, Petitt GD, Woodall JM. 1985. *Appl. Phys. Lett.* 47: 26–28

Annual Review of Materials Science
Volume 25, 1995

CONTENTS

vii

viii   CONTENTS (*continued*)

▷ Keynote Topic: Electronic Materials